

# 1 Probabilistic Liquefaction-Induced Lateral Spread Hazard 2 Mapping and its Application to Utah County, Utah

3  
4 Mahyar Sharifi-Mood <sup>a)</sup>, Daniel T. Gillins <sup>b)</sup>, Kevin W. Franke <sup>c)</sup>, Jasmyn N. Harper <sup>d)</sup>,  
5 Steven J. Bartlett <sup>e)</sup>, and Michael Olsen <sup>a)</sup>

6  
7 Corresponding (first) author: Mahyar Sharifi Mood, Kearney Hall, 1491 SW Campus Way  
8 Corvallis, Oregon 97331-3212, Phone: 917-703-8456, E-mail address: Mahyar.sh@gmail.com

## 10 Abstract

11 Earthquake-induced liquefaction may result in the lateral spread displacement of soil  
12 down gently sloping ground or towards a free-face, causing severe and costly damage to  
13 various facilities, bridges, buildings and other critical infrastructure. Despite the availability  
14 of analytical methods, most engineers currently use empirical or semi-empirical regression  
15 models to estimate liquefaction-induced lateral spread displacements at specific sites.  
16 However, the application of these regression models for regional mapping over a large  
17 geographic areas can be difficult because of challenges associated with the adequate  
18 characterization of subsurface soil and groundwater conditions, geotechnical properties,  
19 regional topography, and uncertainties associated with the causative seismic loading. To

---

<sup>a</sup> School of Civil and Construction Engineering, Oregon State University, Corvallis, OR 97331 3212, USA

<sup>b</sup> National Geodetic Survey, National Oceanic and Atmospheric Administration, 1315 East-West Highway, Silver Spring, MD 20910, USA

<sup>c</sup> Department of Civil and Environmental Engineering, Brigham Young Univ., Provo, UT 84602, USA

<sup>d</sup> FM Global, 601 108<sup>th</sup> Ave NE, Ste 1400, Bellevue, WA 98004, USA

<sup>e</sup> Department of Civil and Environmental Engineering, University of Utah, 122 S. Central Campus Dr., Salt Lake City, UT 84112, USA

20 address these challenges, this paper presents a new and fully probabilistic procedure for  
21 regional hazard mapping of liquefaction-induced lateral spread displacement. The mapping  
22 process is demonstrated through an implementation in Utah County, Utah. To demonstrate  
23 the type of lateral spread displacement hazard maps possible, maps corresponding to return  
24 periods of 1,033 and 2,475 years are developed for Utah County, Utah. The proposed  
25 procedure incorporates topographical data from airborne lidar surveys and geotechnical and  
26 geological data from available maps and subsurface explorations. It accounts for  
27 uncertainties in the soil properties, seismic loading, and the empirical models for predicting  
28 lateral spread displacement using Monte Carlo simulations.

## 30 1. INTRODUCTION

31 Seismically-induced soil liquefaction occurs as excess pore water pressure generated by cyclic strains  
32 in loose, saturated, and cohesionless soil significantly reduces the shear resistance and stiffness of the soil.  
33 A horizontal movement in the soil above a liquefied subsurface layer is called lateral spread (Youd et al.  
34 2001). This type of movement generally develops on gently sloping ground or in the vicinity of a free-  
35 face (e.g., river channels, canals or abrupt topographical depression). Lateral spreads have historically  
36 resulted in excessive cost and damage to urban communities by rupturing utility lines, destroying  
37 foundations, and straining structures. Recent major earthquakes in New Zealand, Japan, Peru, Chile,  
38 China, and Haiti have highlighted the need for earthquake engineers to be able to assess, delineate, and  
39 quantify the potential for lateral spread hazard when evaluating both new and existing facilities on loose  
40 soil sites.

41 Geotechnical engineers most commonly evaluate liquefaction and lateral spread hazard either  
42 analytically or empirically using site-specific techniques. However, some researchers have attempted to  
43 quantify and map liquefaction and ground displacement hazard across a larger region (such as a county)  
44 in an effort to produce preliminary hazard evaluation for planning, engineering and development  
45 purposes. Early liquefaction hazard mapping efforts were generally qualitative and based largely on

46 liquefaction susceptibility correlations with mapped surficial geology. These were implemented out of  
47 necessity due to insufficient subsurface soil and groundwater information, or lack of development of  
48 predictive models that incorporated important site and soil factors (e.g., Youd and Hoose 1977; Youd and  
49 Perkins 1978). Later, liquefaction potential mapping efforts (e.g., Anderson et al. 1982; Baise et al. 2006)  
50 began considering regional seismic loading in addition to liquefaction susceptibility correlations with  
51 mapped surface geology to characterize the regional liquefaction triggering hazard. The additional  
52 evaluation of the available subsurface geotechnical information across a region in the liquefaction hazard  
53 mapping process (e.g., Anderson et al. 1982; Baise et al. 2006; Lenz and Baise 2007; Olsen et al. 2007;  
54 Gillins 2012) improved the characterization of the liquefaction triggering hazard. These approaches  
55 typically used the results for the “critical layer” (i.e., the layer of soil with the smallest factor of safety  
56 against liquefaction triggering) in the soil profile to define the liquefaction hazard. However, other  
57 researchers have quantified this hazard using a different metric such as liquefaction potential index (LPI)  
58 (e.g., Iwasaki et al. 1982; Luna and Frost 1998; Holzer et al. 2006; and Cramer et al. 2008), liquefaction  
59 risk index (LRI) (e.g., Lee et al. 2004; Sonmez and Gokceoglu 2005) or **liquefaction severity index (LSI)**  
60 (e.g., Youd and Perkins 1987). Each of these indices are calculated by integrating the liquefaction  
61 triggering potential across all potentially liquefiable soil layers at a site to a single value.

62 While integrated liquefaction hazard metrics such as LPI, LSI and LRI have proven useful in  
63 mapping the liquefaction triggering hazard across a region, they have been shown to correlate rather  
64 poorly with observed lateral spread displacements following major earthquake events because of other  
65 relevant factors such as site topography and spatial continuity that are not accounted for in their  
66 computation (Maurer et al. 2014; Rashidian and Gillins 2018). Other investigators have developed lateral  
67 spread displacement hazard maps using correlations with mapped surface geology (e.g., Youd and Perkins  
68 1978) or empirical displacement prediction models in the mapping procedure (e.g., Mabey and Madin  
69 1993, Olsen et al. 2007; Gillins 2012; Jaimes et al. 2015). These latter displacement hazard maps were  
70 developed from a single earthquake scenario developed from either a deterministic seismic hazard  
71 analysis or a probabilistic seismic hazard analysis at a single return period. However, these maps do not

72 consider seismic loading from multiple seismic sources and across multiple return periods, nor do they  
73 account for variation in ground motion amplification from site response effects (e.g., Bazzurro and  
74 Cornell 2004; Stewart et al. 2014).

75 This study presents a new and comprehensive procedure to develop fully probabilistic lateral spread  
76 hazard prediction maps that account for uncertainties in ground motions, site response, subsurface  
77 geotechnical and groundwater information, and lateral spread displacement prediction models. This  
78 procedure is based on a performance-based earthquake engineering framework that incorporates  
79 probabilistic seismic hazard analysis (PSHA) of the region, site geology base maps, available subsurface  
80 geotechnical investigations, available groundwater data, and high-resolution light detection and ranging  
81 (lidar) topographic data. The proposed methodology is demonstrated for a study area in Utah County,  
82 Utah, resulting in probabilistic lateral spread displacement hazard maps for the area corresponding to the  
83 return periods of 1033 and 2475 years.

## 84 **2. PREDICTION OF LATERAL SPREAD DISPLACEMENTS**

85 Currently, lateral spread displacement prediction methods can be divided into three generalized  
86 categories (Franke 2005): (1) empirical prediction models based solely on field data and observation (e.g.,  
87 Hamada et al. 1986; Bartlett and Youd 1995; Rauch and Martin 2000; Bardet et al. 2002; Youd et al.  
88 2002; Gillins and Bartlett 2013); (2) semi-empirical prediction models based on theoretical derivation that  
89 are calibrated against laboratory and/or field data (e.g., Zhang et al. 2004; Faris et al. 2006; Idriss and  
90 Boulanger 2008); and (3) analytical prediction models that numerically compute displacements and that  
91 are based on the mechanics of the liquefaction and/or horizontal ground deformation (e.g., Bray and  
92 Travasarou 2007; Seid-Karbasi and Byrne 2007; Saygili and Rathje 2008; Lam et al. 2009). Despite the  
93 fact that analytical methods continue to make significant progress in their ability to accurately predict  
94 lateral spread displacements, empirical and semi-empirical prediction models remain the most popular  
95 method for predicting lateral spread displacements among engineering practitioners today because of their  
96 simplicity, familiarity, and basis in field performance from case histories of lateral spread (Franke and  
97 Kramer, 2014). However, a large amount of aleatory uncertainty is usually associated with these types of

98 predictive models, or in fact with any type predictive model, because of the complexities of the  
99 subsurface geology and lateral spread phenomenon and the paucity of well-documented lateral spread  
100 case histories for developing robust empirical models.

101 Bartlett and Youd (1995) originally considered lateral spread events from earthquakes in Japan and  
102 the western United States and statistically regressed an empirical prediction model from their resulting  
103 case history data that included earthquake moment magnitude, source-to-site distance, several  
104 geotechnical soil factors, and slope geometry. Later, Youd et al. (2002) updated their lateral spread case  
105 history database and developed a revised multilinear regression prediction model, which remains widely  
106 used by engineering practitioners today. Recently, Gillins and Bartlett (2013) simplified the Youd et al.  
107 (2002) prediction model by consolidating some of the required geotechnical input factors such as fines  
108 content and mean grain size into a single soil classification factor. The Gillins and Bartlett (2013) model  
109 was developed specifically for lateral spread hazard mapping applications because it does not require  
110 laboratory test results for the soil but instead relies upon visual soil classifications, which are more readily  
111 available in most geotechnical field boring logs. The Gillins and Bartlett (2013) multilinear regression  
112 empirical model is given as:

$$113 \quad \log D_H = b_0 + b_1 M_W + b_2 \text{Log } R^* + b_3 R + b_4 \text{Log } W + b_5 \text{Log } S + b_6 \text{Log } T_{15,cs} + 0.252 + \varepsilon \quad (1)$$

114 where  $D_H$  is the permanent estimated horizontal lateral spread displacement in meters;  $M_W$  is the moment  
115 magnitude of the earthquake;  $R$  is the closest horizontal distance in kilometers from the site to the vertical  
116 surface projection of the fault rupture (i.e., the Joyner-Boore distance,  $R_{JB}$ );  $W$  is the free-face ratio (i.e.,  
117 the ratio of the height to the horizontal distance from the site to the toe of the slope) in percent (%);  $S$  is  
118 the slope gradient in percent (%); and  $R^*$  is a distance parameter used to characterize near-source  
119 earthquakes and is computed as:

$$120 \quad R^* = R + 10^{0.89M_W - 5.64} \quad (2)$$

121  $T_{15,cs}$ , which is the only geotechnical variable in Equation (1), is the clean-sand equivalent value  
122 for  $T_{15}$ , and is computed as:

123 
$$T_{15,cs} = T_{15} \cdot 10^{\left(\frac{-0.683 x_1 - 0.200 x_2 + 0.252 x_3 - 0.040 x_4 - 0.535 x_5 - 0.252}{0.592}\right)} \quad (3)$$

124 where  $T_{15}$  is the cumulative thickness (in meters) of saturated, cohesionless, and continuous soil deposits  
 125 in the upper 15 meters of the soil profile with corrected standard penetration test (SPT)  $(N_1)_{60} < 15$   
 126 hammer blows per 0.3 meter, and  $x_n$  is the ratio of the cumulative thickness (in meters) of soil with a  
 127 **Soil Index (SI) value  $n$**  with  $(N_1)_{60} < 15$  to the total  $T_{15}$  for the entire soil column. Thus,  $x_n$  will range  
 128 between 0 and 1, and the sum of  $x_1$  through  $x_5$  will equal 1. *SI* values and their definitions are provided  
 129 in Table 1.

130 **Table 1. Soil Index (SI) values and their definitions** (from Gillins, 2012).

<i>SI</i>	Definition
1	Silty gravel with sand, silty gravel, fine gravel
2	Coarse to very coarse sand, sand and gravel, gravelly sand
3	Sand, medium to fine sand, sand with some silt
4	Fine to very fine sand, sand with silt, silty sand, dirty sand
5	Sandy silt, silt with sand
6	Non-liquefiable, such as cohesive soil or soil with high plasticity

131  
 132 Using the Youd et al. (2002) lateral spread case history database, Gillins and Bartlett (2013) solved  
 133 for the regression coefficients,  $b_0$  to  $b_6$ , for Equation (3). These coefficients are given in Table 2  
 134 according to the topographic conditions at a site. The error for the regression model,  $\varepsilon$ , is normally  
 135 distributed with a mean of 0.0 and a standard deviation,  $\sigma_{\log D_H} = 0.2232$  and the coefficient of  
 136 determination,  $R^2$  is 79.0%.

137  
 138 **Table 2. Gillins and Bartlett (2013) empirical regression model coefficients for lateral spread**  
 139 **displacement prediction**

Model	$b_0$	$b_1$	$b_2$	$b_3$	$b_4$	$b_5$	$b_6$
Ground - Slope	-8.208	1.318	-1.073	-0.016	0	0.337	0.592
Free Face	-8.552	1.318	-1.073	-0.016	0.445	0	0.592

140

### 3. PERFORMANCE-BASED PREDICTION OF LATERAL SPREAD

#### DISPLACEMENTS

Earthquake scientists and engineers have long recognized that many uncertainties exist associated with predicting earthquake ground motions and their subsequent effects on the ground and structures. In response, these professionals have developed and implemented probabilistic or performance-based earthquake engineering design procedures, which quantify and account for as many of the uncertainties associated with the evaluation as possible. These procedures typically quantify the associated hazard in terms of a mean annual rate of exceedance,  $\lambda$ .

Franke and Kramer (2014) introduced a performance-based procedure built upon the probabilistic framework introduced by the Pacific Earthquake Engineering Research Center (PEER; Cornell and Krawinkler 2000; Deierlein et al. 2003) to compute the mean annual rate of exceeding some lateral spread displacement,  $d$ . Their procedure modifies the Youd et al. (2002) model by grouping together all of the model variables related to seismic loading (i.e.,  $M_W$  and  $R$ ) and designating them as the apparent loading parameter,  $\mathcal{L}$ . Because  $\mathcal{L}$  is a function of parameters  $M_W$  and  $R$ , it is analogous to a ground motion attenuation relationship and can be treated in a similar manner. Likewise, the Franke and Kramer procedure groups together all of the model variables related to local site conditions (i.e.,  $S$ ,  $W$ ,  $T_{15}$ , fines content, and mean grain size) and designates them as a site parameter,  $G$ .

A similar modification can be applied to the Gillins and Bartlett (2013) model presented in Eq. 1. In this modified form of the model, the apparent loading parameter is defined as:

$$\mathcal{L} = b_1 M_W + b_2 \text{Log } R^* + b_3 R \quad (4)$$

The modified site parameter is defined as:

$$G = -(b_0 + b_4 \text{Log } W + b_5 \text{Log } S + b_6 \text{Log } T_{15,cs} + 0.252) \quad (5)$$

The model error is defined as:

$$\varepsilon = \sigma_{\log D_H} \Phi^{-1}[P] \quad (6)$$

165 where  $\Phi^{-1}$  is the inverse standard normal cumulative distribution function, and  $P$  is the probability of  
 166 exceeding the median predicted lateral spread displacement,  $\widehat{D}_H$ . Using this modified syntax, Equation (1)  
 167 can be re-written as:

$$168 \quad \log D_H = \mathcal{L} - G + \varepsilon \quad (7)$$

169 As demonstrated by Franke and Kramer (2014), the modified lateral spread model can now be  
 170 inserted into a performance-based framework to compute the mean annual rate of exceeding a specific  
 171 lateral spread displacement  $d$  as:

$$172 \quad \lambda_d = \sum_{i=1}^{N_{\mathcal{L}}} P[D_H > d \mid G, \mathcal{L}_i] \Delta \lambda_{\mathcal{L}_i} \quad (8)$$

173 Where  $N_{\mathcal{L}}$  is the number of bins or increments associated with the seismic hazard curve for  $\mathcal{L}$  developed  
 174 through a probabilistic seismic hazard analysis (PSHA);  $\Delta \lambda_{\mathcal{L}_i}$  is the size of each hazard increment or bin  
 175 associated with the seismic hazard curve for  $\mathcal{L}$ ; and  $P[D_H > d \mid G, \mathcal{L}_i]$  is the conditional probability that  
 176 the median predicted lateral spread displacement exceeds displacement  $d$  conditional upon seismic  
 177 loading  $\mathcal{L}_i$  and constant site conditions  $G$ . If the model error term,  $\varepsilon$ , is removed or neglected, Equation  
 178 (1) will produce the mean value of  $\log D_H$  (i.e.,  $\overline{\log D_H}$ ), and the conditional probability term shown in  
 179 Equation (8) can be computed as:

$$180 \quad P[D_H > d \mid G, \mathcal{L}_i] = 1 - \Phi \left[ \frac{\log d - \overline{\log D_H}}{\sigma_{\log D_H}} \right] = 1 - \Phi \left[ \frac{\log d - \overline{\log D_H}}{0.2232} \right] \quad (9)$$

181 One of the advantages of the Franke and Kramer (2014) formulation of an empirical lateral  
 182 spread model is that it distinguishes the seismic loading from the site parameters in the calculation of  
 183 lateral spread displacement. By doing so, the procedure allows for  $\mathcal{L}$  to be evaluated in a PSHA before  
 184 any site-specific geotechnical or topographic information is available, thus resulting in a seismic hazard  
 185 curve for  $\mathcal{L}$ . If all of the uncertainty from the lateral spread prediction (i.e.,  $\sigma_{\log D_H}$ ) is assigned to  $\mathcal{L}$  in the  
 186 PSHA, then site-specific and probabilistic estimates of lateral spread displacement can be immediately  
 187 computed once geotechnical and topographic information from the site become available.



188           Given that a seismic hazard curve for  $\mathcal{L}$  can be developed for a given site through a PSHA that  
189 incorporates Equation (4) before any site-specific soil and/or topographic information is available, it is  
190 then possible to develop a series of hazard curves for  $\mathcal{L}$  across a geographic grid of points for the purpose  
191 of lateral spread displacement hazard mapping. Because the development of the  $\mathcal{L}$  hazard curve is  
192 computationally expensive, the grid spacing at which the hazard curves are developed should be carefully  
193 considered. Ulmer et al. (2015) evaluated this problem and recommended grid spacing for the mapping of  
194 lateral spread displacement hazard as a function of mapped probabilistic values of peak ground  
195 acceleration (PGA) at a return period 2,475 years from the U.S. Geological Survey (USGS) National  
196 Seismic Hazard Mapping Project (NSHMP). If PGA values at this return period exceed 0.64 g, then  
197 Ulmer et al. (2015) recommend a minimum grid spacing of 4 km.

#### 198           **4. CORRELATION OF REGIONAL GEOTECHNICAL PROPERTIES TO** 199           **MAPPED SURFACE GEOLOGY**

200           Equations (8) and (9) provide a performance-based framework to compute the mean annual rate of  
201 exceeding a particular lateral spread displacement,  $d$ , given a site geometry,  $G$ . Unfortunately, when  
202 mapping lateral spread displacement across a regional area using only available geotechnical data,  $G$  is  
203 highly uncertain due to the paucity of geotechnical drilling, sampling, and testing across the area. **Since**  
204 **this problem often occurs in practice, this paper assumes there is generally a lack of available data to be**  
205 **able to spatially interpret geotechnical variables or develop a continuous ground water table model**  
206 **through a highly dense number of subsurface investigations, like done in other hazard mapping methods**  
207 **for smaller study areas (e.g., Liu et al. 2016; Juang et al. 2017; Baker et al. 2008; Chen et al. 2016). To**  
208 **deal with this problem and account for the high uncertainty in  $G$  across the region area of interest with**  
209 **limited geotechnical investigations, Monte Carlo simulations can be used to develop a range of  $T_{15,c5}$  for**  
210 **given geologic units.**

211           Sharifi-Mood (2017) describes a procedure in which subsurface geotechnical exploration data and  
212 groundwater levels can be collected across the regional area of interest and correlated to mapped surface

213 geology. SPT boring logs and CPT soundings can be collected from publicly available sources, as well as  
214 solicited from private consultants and owners, to develop a geotechnical subsurface database for the area.  
215 These subsurface explorations can then be grouped according to mapped surface geology within the  
216 database. For a given geologic unit, all logged soil properties for each *SI* defined in Table 1 are gathered  
217 together, and histograms and corresponding probability density functions (PDFs) are developed for each  
218 available or measured soil property including unit weight, moisture content, and Atterberg limits. By thus  
219 grouping together the soils from each geologic unit and developing histograms for the available soil  
220 properties based on *SI* type, a Monte Carlo simulation can be used in the performance-based lateral spread  
221 hazard mapping procedure to randomly generate a soil profile and groundwater level that is consistent  
222 with any particular geologic unit of interest. The application of such a Monte Carlo simulation will be  
223 described in greater detail below.

224         Some discussion is warranted regarding the validity and applicability of correlating geotechnical  
225 properties to mapped surface geology. An ideal geotechnical sampling scheme for this type of approach  
226 would involve selecting a sufficient number of geotechnical explorations in each mapped geologic unit  
227 and spacing them sufficiently to capture the spatial uncertainty of the soil deposits within each geologic  
228 unit, particularly the “critical” liquefying soil deposit(s) that governs lateral spread behavior.  
229 Unfortunately, planning and implementing such a sampling scheme for the purpose of liquefaction and/or  
230 lateral spread displacement hazard mapping constitutes a significant effort and financial cost, and is  
231 therefore unfeasible for most researchers. Instead, most researchers must rely upon that geotechnical  
232 exploration data that is already available to them through public records and/or donation by private  
233 owners. As such, reliance upon such geotechnical exploration data is certain to result in the under-  
234 sampling of certain geologic units and geographic areas, the spatial clustering of geotechnical  
235 explorations along various infrastructure features such as highways, and an elevated risk of inconsistent  
236 and/or incorrect soil logging. **Such paucity of data and inconsistency in sampling strategies also makes it**  
237 **difficult to spatially interpolate the data between investigations.** However, given that liquefaction and  
238 lateral spread hazard maps are intended to be a preliminary assessment tool for engineers and decision-

239 makers, and in no way are intended to supersede or replace site-specific liquefaction hazard analysis, such  
240 short-comings of the geotechnical database are both understandable and necessary.

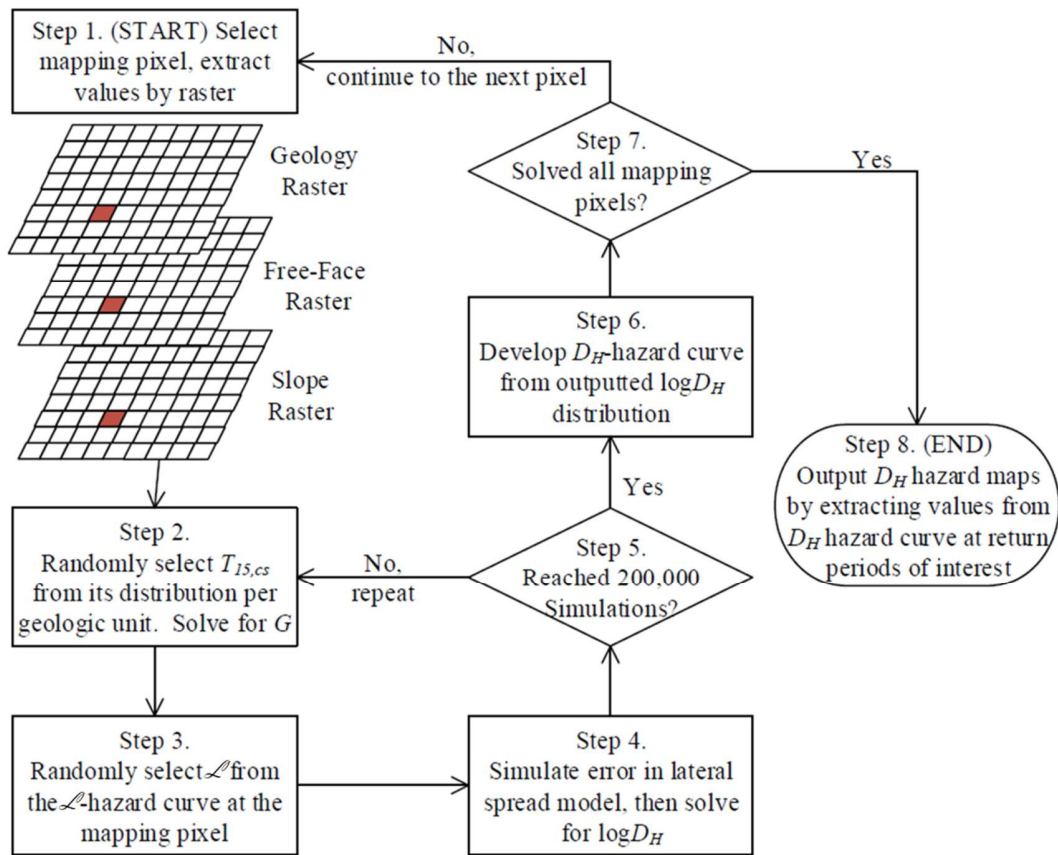
241

## 242 **5. PROPOSED PERFORMANCE-BASED LATERAL SPREAD HAZARD** 243 **MAPPING PROCEDURE**

244 The proposed performance-based lateral spread hazard mapping procedure requires several inputs  
245 related to seismic loading, surface topography, and subsurface geotechnical properties across the region  
246 of interest. Most of these inputs come in the form of a digital raster, which consists of a matrix of pixels  
247 organized into rows and columns where each pixel contains a value representing information. The inputs  
248 required for the performance-based lateral spread hazard mapping procedure are as follows: (1) a raster of  
249 the mapped surface geology of the study area; (2) rasters of the ground slope and free-face ratios  
250 computed from a high-resolution digital elevation model (DEM); (3) a geotechnical database comprised  
251 of as many SPT logs and CPT soundings from as many of the mapped geologic units in the study area as  
252 possible; and (4) rasters of the seismic hazard curves for  $\mathcal{L}$ , developed from a series of PSHAs performed  
253 across the study area. The incorporation of these inputs for the development of performance-based lateral  
254 spread displacement hazard mapping procedure is illustrated in a flow chart diagram in Figure 1. Each  
255 step of this flow chart is briefly summarized below.

256 For the proposed mapping procedure summarized in Figure 1, the lateral spread hazard is  
257 computed for each individual pixel of a raster of the study area. The process is repeated for each pixel,  
258 and the results at each pixel are then combined to produce the final hazard maps. To accelerate the  
259 computations, the pixels can be evaluated simultaneously using parallel processing. However, for clarity,  
260 this paper will describe the process as if solving for the hazard at each pixel sequentially.

261



262

263 **Figure 1.** Proposed procedure for producing performance-based lateral spread displacement hazard maps

264

265 Step 1: Extract Raster Data at a Map Pixel:

266 Because the geology and depositional environment significantly influences the susceptibility of the  
 267 soil to liquefaction, the proposed mapping method begins by utilizing available surface geology maps.  
 268 These maps are compiled, digitized, georeferenced, and converted into a raster image for the mapping  
 269 area.

270 In addition to developing a raster image of the surface geology of the mapping area, additional  
 271 rasters are developed to describe the spatial variation in site geometry in the mapping area. Using a  
 272 DEM, raster images of the percent ground slope, and proximity and depth of free-faces are computed.  
 273 (Note that an example of computing these rasters is given in the following section.)

274 For the proposed mapping method, the lateral spread hazard is computed for each individual pixel  
275 of a raster in the mapping area. As illustrated in Figure 1, beginning at one pixel in the mapping area, the  
276 raster values from the surface geology, slope ( $S$ ), and free-face ( $W$ ) rasters are extracted at that location.

277

278 Step 2: Begin Monte Carlo Simulations, Compute  $T_{15,cs,i}$ :

279 Step 2 initiates a Monte Carlo simulation to account for uncertainty in the geotechnical properties and  
280 seismic loading at the pixel of interest. Given the mapped surface geologic unit for a given pixel being  
281 analyzed, a random geotechnical exploration (i.e., SPT log) is selected from the geotechnical database  
282 according to the mapped geologic unit. Soil properties that are missing or are not specified on the  
283 randomly selected log or sounding are randomly created from the histograms developed as part of the  
284 geotechnical database. While soil factors such as moisture content, fines content, Atterberg limits and dry  
285 unit weights are simulated, neither SPT N values nor soil types are simulated because only geotechnical  
286 explorations with these data listed with depth are used. Once a complete soil profile is available with SPT  
287 N values, soil layering with descriptions, and moisture content, fines content, dry unit weights, and  
288 Atterberg limits for each layer, then total and effective stress profiles are computed and the SPT N values  
289 are corrected to  $(N_1)_{60}$  values. Then, a value for  $SI$  is assigned to each layer in the soil profile and a value  
290 of  $T_{15,cs}$  is computed using Equation (3). For an example of how to compute  $T_{15,cs}$  from an SPT log, refer  
291 to Gillins and Bartlett (2013).

292 As part of this step, the procedure could be developed so that the random selection of an SPT for each  
293 Monte Carlo simulation is weighted based on the distance of the pixel of interest to the location of the  
294 available SPTs in the geotechnical database. A higher weight for random sampling could be given to  
295 nearer SPTs, since the soil profile is likely to be similar to the profile from nearby SPT(s). This approach  
296 would also ensure that if the pixel is located at the location of an SPT in the database, it uses the soil log  
297 from this SPT. Gillins (2012) developed a semivariogram of  $T_{15,cs}$  for all boreholes in a geotechnical  
298 database and used this semivariogram as a basis for developing a weighting scheme. However, the

299 semivariogram reached a sill at only 30 m. Thus, the pixel must be very close to an SPT for spatial  
300 correlation with its measured value for  $T_{15,cs}$ .

301 The computed value of  $T_{15,cs}$  is then assigned to the  $i$ -th iteration of the Monte Carlo simulation as  
302  $T_{15,cs,i}$ , and it is used in later steps to compute the corresponding lateral spread displacement for the  $i$ -th  
303 iteration.  $T_{15,cs,i}$  is then combined with topographic parameters  $S$  and  $W$  associated with the pixel of  
304 interest and that were obtained in Step 1, and values of  $G_i$  are computed for both the free face and ground-  
305 slope conditions using Equation (5) and Table 2.

306

307 Step 3: Develop Apparent Loading Parameter Value,  $\mathcal{L}_i$ :

308 Continuing with the  $i$ -th simulation, Step 3 randomly selects an apparent loading parameter value  
309 based on its corresponding likelihood. For each pixel, the corresponding hazard curve for  $\mathcal{L}$  is first  
310 transformed to a PDF using the procedure presented by Bazzurro and Cornell (2004). A value of  $\mathcal{L}$  is then  
311 randomly selected from the PDF according to its relative likelihood and is combined with  $G_i$  from Step 2  
312 for the computation of  $\log D_H$ .

313 The description above assumes that the series of PSHAs performed across the study area  
314 computes hazard curves for  $\mathcal{L}$  at every pixel in mapping raster. However, the raster pixel spacing for  
315 mapping is commonly much smaller (e.g., 30 meters) than the grid spacing for regional PSHA  $\mathcal{L}$  due to  
316 the extensive number of calculations the PSHA typically requires. If such is the case, then an interpolation  
317 scheme must be performed to develop hazard curves of  $\mathcal{L}$  for each pixel in the raster. Under this  
318 condition, a hazard curve for  $\mathcal{L}$  can be derived through bilinear interpolation of the nearest gridded  $\mathcal{L}$   
319 hazard curves surrounding the pixel of interest.

320

321 Step 4: Compute  $\log D_H$

322 The final step in  $i$ -th iteration of the Monte Carlo simulation is to solve Equation (7). The subtracting  
323  $G_i$  from Step 2 from the selected value for  $\mathcal{L}_i$  from Step 3 produces  $\overline{\log D_{Hi}}$  for the iteration. A value for

324 the error in the lateral spread displacement model,  $\varepsilon$ , is then simulated using a random number generator  
 325 that follows the standard normal distribution.

326 Equation (7) can now be rewritten to compute  $[\log D_H]_i$  for the  $i$ -th iteration at a mapping pixel as:

$$327 \quad [\log D_H]_i = \overline{\log D_{H_i}} + \varepsilon = \overline{\log D_{H_i}} + \sigma_{\log D_H} \cdot K_{rand,i} = \overline{\log D_{H_i}} + 0.2232 K_{rand,i} \quad (10)$$

328 where  $K_{rand,i}$  is a random value generated from the standard normal distribution for the  $i$ -th simulation.

329 Step 5: Repeat Steps 2 – 4 for Required Number of Simulations

330 Step 5 involves repeating Steps 2 through 4 until a full probability distribution of  $[\log D_H]$  is  
 331 developed at the selected pixel. Development of a full probability distribution requires that an adequate  
 332 number of iterations must be performed to fully characterize the major sources of uncertainty in the  
 333 process. We observed that 200,000 simulations is generally sufficient to develop an adequate probability  
 334 distribution of  $[\log D_H]$  at each pixel. Upon completion of all of the simulations, the probability  
 335 distribution for  $[\log D_H]$  is transformed to a probability distribution for  $D_H$  values (in meters) for each  
 336 pixel by raising each  $[\log D_H]$  value by the power of 10.

337

338 Step 6: Develop a  $D_H$  Hazard Curve:

339 In Step 6, the probability distribution for  $D_H$  is transformed into a hazard curve for  $D_H$  at each pixel.  
 340 The probability distribution for  $D_H$  is first transformed into a cumulative distribution function (CDF) for  
 341  $D_H$  through numerical integration. Then using the Poisson probability model, the mean annual rate of  
 342 exceeding some lateral spread displacement  $d$  (i.e.,  $\lambda_d$ ) is computed as:

$$343 \quad \lambda_d = -\frac{\ln[1-F(d)]}{t=1} = -\ln[1 - F(d)] \quad (11)$$

344 where  $t$  is exposure period in years and is equal to unity to solve for the mean annual rate of exceedance,  
 345 and  $F(d)$  is the CDF function corresponding to the displacement  $d$ .

346

347 Step 7: Repeat Previous Steps for All Mapping Pixels:

348 Each of the first six steps are repeated for every pixel in the study area, resulting in hazard curves for  
349  $D_H$  at every pixel.

350

351 Step 8: Output Maps for Desired Return Periods:

352 In Step 8, values of  $D_H$  are extracted from the hazard curves at a user-defined return period (e.g., 475,  
353 1,033, or 2,475 years [10%, 5% and 2% in 50 years]) for each mapping pixel. The extracted value at each  
354 pixel can be aggregated into a raster image, and this image is then used to develop a lateral spread  
355 displacement hazard map at the desired return period.

356

357 **6. IMPLEMENTATION OF THE MAPPING METHOD FOR UTAH COUNTY,**

358 **UTAH**

359 As an example to clarify the proposed mapping method, the flow chart illustrated in Figure 1 was  
360 followed to produce lateral spread displacement hazard maps for Utah County, Utah. Utah County is the  
361 second-most populous county in the state of Utah and comprises a significant portion of the overall state  
362 and regional economies. However, the liquefaction hazard is considered significant in that portion of the  
363 county due to its close proximity to high seismic (e.g., the Wasatch fault) and surficial water (e.g., Utah  
364 Lake) sources, shallow ground water tables, and widespread granular and/or silty soils in the upper 5 to  
365 15 meters of sediments. Development of fully probabilistic liquefaction-induced lateral spread  
366 displacement hazard maps for the county will provide a tool for agencies, planners, departments, and  
367 engineers to identify and prioritize locales where future site-specific liquefaction studies should be  
368 performed.

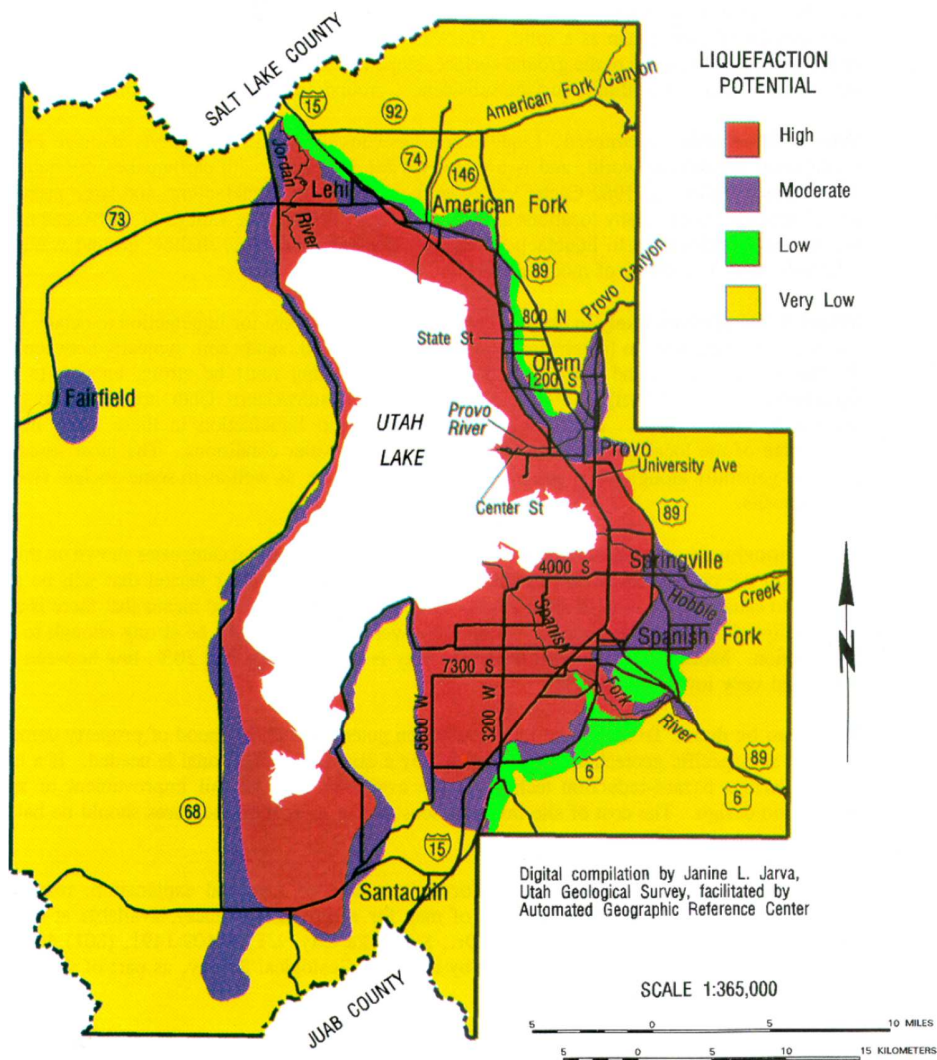
369 Anderson et al. (1982) previously developed a method to map liquefaction triggering potential for  
370 urban areas in twelve counties in Utah, including Utah County (Anderson et al. 1994a,b). To produce  
371 these maps, Anderson et al. computed the potential for liquefaction triggering at available SPT borehole  
372 and CPT sounding locations. They determined critical acceleration values needed to trigger liquefaction



373 using a method introduced by Seed (1979). They then compared these critical accelerations to  
374 probabilistic predictions from seismic hazard analyses. Using surficial geologic maps as constraints, they  
375 generalized the results at each geotechnical investigation and produced qualitative liquefaction potential  
376 maps delineating zones of *low*, *moderate*, and *high* liquefaction potential. The Anderson et al. (1994a,b)  
377 hazard map of Utah County (see Figure 2) shows high liquefaction potential for most of the urban area in  
378 the county. Although this map is a useful reference for liquefaction triggering, it is dated and does not  
379 estimate liquefaction effects such as lateral spread displacement.

380 To accomplish the 8 steps of the mapping method shown in Figure 1 and summarized above,  
381 available data were compiled into a geospatial database, custom MATLAB scripts were written to  
382 perform the computations, and Esri's ArcMap® was used to visualize and analyze the outputs. This  
383 database is a portion of a larger geospatial database in state of Utah, GeoDU which has been compiled  
384 and used in other liquefaction mapping efforts (Gillins and Franke 2016, Sharifi-Mood 2017, Gillins  
385 2012; Olsen et al. 2007; Erickson 2006; Bartlett and Gillins 2013). The following narrative provides  
386 details of each of the 8 steps of the mapping process, including the source of the data inputs and  
387 identification of any key assumptions. For additional details on the new Utah County liquefaction hazard  
388 maps, see Gillins and Franke (2016).

389



390  
 391 **Figure 2.** Previous qualitative liquefaction potential hazard map developed by Anderson et al. (1994a,b)  
 392 (reprinted with permission from the Utah Geological Survey)  
 393

394 **Step 1: Input Geology, Slope, and Free-Face Data**

395 A vector-based geology base map of the study area (Constenius et al. 2011) was obtained from the  
 396 Utah Geological Survey and input into a geospatial database. The Constenius et al. (2011) map is a  
 397 compilation of detailed and recent mapping of several 7.5-minute quadrangles at 1:24,000 to 1:50,000-  
 398 scale along part of the populous Wasatch Front and Utah Valley. Figure 3 presents the study area in Utah  
 399 County and illustrates the surficial geologic units mapped by Constenius et al. (2011) with overlain

400 locations of geotechnical explorations for the study, which will be discussed in Step 2 below. Holocene to  
401 Upper Pleistocene alluvial, lacustrine, and deltaic deposits are primarily shown on the map. Based on  
402 Youd and Perkins (1978), these deposits are moderately to very highly susceptible to liquefaction. The  
403 figure also depicts the Wasatch Mountains which bound the study area on the east, the Utah segment of  
404 the Wasatch Fault Zone (the primary seismic threat in Utah County), the extents of Utah Lake, and West  
405 Mountain to the south of Utah Lake. The study area is also bounded on the west by the Lake Mountains.

406 The authors grouped the quaternary geologic units in the study area into 14 categories, as tabulated in  
407 Table 3. Table 3 provides the symbol, description, and age for each of the units within the 14 categories  
408 from the Constenius et al. (2011) map. The geologic units depicted in Figure 3 were then converted into a  
409 raster image, with values ranging from 1 to 14 corresponding to the definitions given in Table 3.

410 A 0.5-meter raster-based DEM of the study area was then downloaded from the Utah Automated  
411 Geographic Research Center (AGRC) (AGRC 2014), and it was stored in the geospatial database. AGRC  
412 developed this DEM from aerial lidar data acquired in the fall of 2013 and the spring of 2014. The high-  
413 resolution DEM was useful for identifying slopes and free-faces in the study area. The ground slope (in  
414 percent) was computed, and the locations of the major free-faces in the study area were digitized. The  
415 Jordan and Provo River and some of their tributaries were considered as free-face features. Besides these  
416 river channels, areas that showed a dramatic change in elevation, which could be readily noticed when  
417 evaluating a hillshade of the DEM, were also digitized as free-face features.

418 During the digitization of the free-face features, a polyline feature class was drawn along the toe of  
419 that the identified free-face, and a polygon feature class was drawn to encompass areas above and  
420 affected by this free-face feature. The polyline and polygon feature were then converted to points at a  
421 spacing less than 30 m. For each point within a polygon, multiple free-face ratios to all points along the  
422 toe were computed by dividing the difference in elevation with the horizontal distance from the site to the  
423 toe, and then the maximum free-face value was assigned as per a method in Gillins (2014). After  
424 repeating the process for all points and all free-face features in a custom MATLAB script, a natural

425 neighbor interpolation among the points was used to output another raster that depicts the free-face ratio,  
426  $W$ , for the study area.

427 The rasters of the surficial geology, slope, and free-faces were computed at a 30-m by 30-m pixel  
428 size. The lateral spread hazard was then evaluated for each individual pixel, resulting in final hazard  
429 maps.

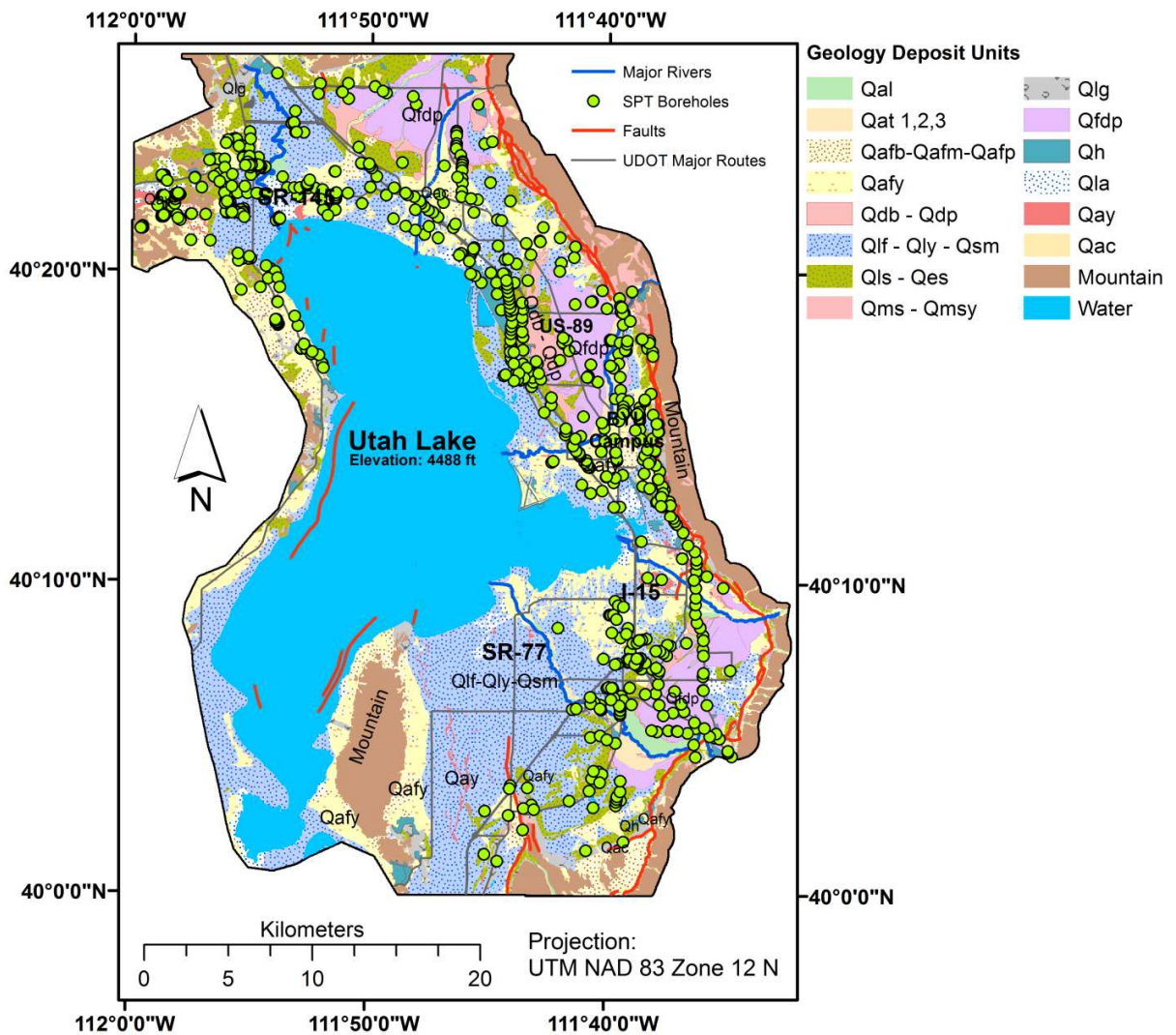


**Figure 3.** Surficial geology and location of SPT boreholes in the study area, Utah County, Utah

433  
434

**Table 3.** Geologic units in study area, descriptions, approximate age, and number of SPT logs.

<b>Deposit Symbol</b>	<b>Description</b>	<b>Age*</b>	<b>#SPT†</b>
<b>1. Stream Alluvium</b>			
Qal	Modern stream alluvium	H	20 (33)
<b>2. Stream-Terrace Alluvium</b>			
Qat <sub>1</sub>	Stream-terrace alluvium, lowest terrace levels	H - UP	4 (7)
Qat <sub>2</sub>	Stream-terrace alluvium, medium terrace levels	H - UP	2 (4)
Qat <sub>3</sub>	Stream-terrace alluvium, highest terrace levels	H - UP	0 (1)
<b>3. Alluvial Fan – Old</b>			
Qafb	Transgressive (Bonneville) Lake Bonneville-age	UP UP to middle	0 (1)
Qafm	Intermediate Lake Bonneville-age alluvial fan	P	6 (21)
Qafp	Regressive (Provo) Lake Bonneville-age alluvial fan	UP	3 (10)
<b>4. Alluvial Fan – Young</b>			
Qafy	Younger alluvial-fan	H	98 (171)
<b>5. Delta</b>			
Qdb	Near Bonneville shoreline of Lake Bonneville	UP	1 (1)
Qdp	Near and below Provo shoreline of Lake Bonneville	UP	5 (13)
<b>6. Fine-Grained Lacustrine</b>			
Qlf	Fine-grained lacustrine from Lake Bonneville	UP	100 (194)
Qly	Young lacustrine less than 6 m thick and overlies Qlf unit	H- UP	4 (6)
Qsm	Fine, organic-rich sediment from springs, marshes, seeps; less than 3 m thick and overlies Qlf unit	H- UP	1 (1)
<b>7. Lacustrine Sand</b>			
Qls	Lacustrine sand below Bonneville and Provo shorelines	UP	58 (100)
Qes	Eolian sand; 1-1.5 m thick and derived from Qls unit	H - UP	4 (7)
<b>8. Landslides</b>			
Qmsy	Modern landslide, currently or recently active	H	3 (6)
Qms	Modern landslide	H	2 (2)
<b>9 – 14. Others</b>			
Qlg	Lacustrine gravel and sand near Bonn. and Provo shorelines	Uppermost P	15 (21)
Qfdp	Lake Bonneville alluvial-fan and delta, Provo stage	Uppermost P	33 (61)
Qh	Human disturbance – fill for major interstate and highways	Historic	45 (53)
Qla	Lacustrine and alluvial, undivided	H – UP	14 (20)
Qay	Alluvial fan and terrace post-Provo shoreline of Lake Bonn.	H – UP	3 (13)
Qac	Alluvium and colluvium, undivided	Quaternary	3 (7)

435  
436  
437  
438

\* = UP = Upper Pleistocene; P = Pleistocene; H = Holocene

† = Number in parenthesis is the grand total of SPTs in the unit. Number outside of parenthesis is the total of SPTs with maximum test depths greater than 7 m (20 ft) and that were actually used in the development of hazard map.

439 **Step 2: Input Geotechnical Data and Compute  $G$**

440 Available geotechnical investigations were collected, digitized, and stored in a geospatial database.  
441 Both SPT borehole logs and CPT soundings were acquired from multiple engineering firms and their  
442 clients, as well as government agencies such as the Utah Department of Transportation (UDOT), Utah  
443 Geological Survey (UGS), Central Utah Water Conservancy District (CUWCD), local city governments,  
444 and private entities. Overall, 753 borehole logs and 39 CPT soundings in the study area were collected,  
445 digitized, and stored in the database. Figure 3 shows the spatial location of each SPT. As can be seen,  
446 numerous tests were found along the Interstate 15 corridor; however, some portions of the county with  
447 limited development (west and just southeast of Utah Lake) have sparser investigations.

448 Data from the SPT and CPT records were input into a database format that was developed and  
449 explained in Gillins (2012). Information such as soil descriptions and classifications, layer delineations,  
450 depths to groundwater, and uncorrected SPT blow counts ( $N_m$ ) from the SPT logs were stored in the  
451 database. In addition, laboratory measurements on soil samples, such as fines contents, Atterberg limits,  
452 unit weights, and moisture contents were digitized. Friction ratio, sleeve friction, cone-tip resistance, and  
453 pore water pressure were stored from the CPT soundings. Most of the CPT soundings also had a pore-  
454 water pressure dissipation test data that gave an estimate of the depth to groundwater.

455 Table 3 shows the total number of SPT borehole logs in each of the 14 geologic categories in the  
456 study area. All 753 logs were used for characterizing the typical soil properties (e.g., moisture content,  
457 Atterberg limits, unit weights) for the geologic units; however, a large number of the tests (329) were  
458 quite shallow, and there was concern that some tests may not have encountered all of the soil layers at  
459 deeper depths which may liquefy and cause ground failures. Although all tests were used to characterize  
460 the geotechnical properties of the soil in Utah County, only SPTs that extended beyond a depth of 7 m  
461 were used when mapping the liquefaction hazard. Table 3 also provides a count of the number of SPT  
462 logs that reached a minimum depth of 7 m in all 14 geologic categories in the study area. A large number  
463 of SPT logs were available for the common units that cover the majority of the study area (e.g., Qafy, Qlf,  
464 Qfdp, Qls). Some of the units have a small number of SPT logs (e.g., Qms, Qat, Qd); however, one

465 reason for this lack of sampling is because these units are rare in the study area. Future tests in under-  
466 developed portions of the study area, or in the geologic units with limited testing would undoubtedly  
467 improve the accuracy of the hazard maps. Future tests could be added to the Utah County geotechnical  
468 database, and new maps could then be produced that refine the maps presented in this paper.

469 A minimum termination depth of 7 m was chosen only as a compromise due to the limitations of  
470 the geotechnical database for Utah County. On one hand, overly shallow borehole tests may not have  
471 captured all of the layers of soil at a site that may liquefy during a major earthquake. On the other hand,  
472 if a deeper threshold was chosen, such as say 20 m, then over 300 of the SPT logs in the geotechnical  
473 database would have been screened out from the mapping process. In order to maintain as many available  
474 logs as possible for mapping the large study area while minimizing the use of overly shallow SPT logs, a  
475 threshold depth of 7 m was ultimately chosen.

476 During this step of the mapping process, a Monte Carlo simulation was initiated and a SPT  
477 borehole log was randomly selected from the total number of SPT logs that reached a minimum depth of  
478 7 m in the geologic category for the selected pixel. For example, if the selected pixel was located in  
479 stream alluvium (i.e., Qal), then one of the 20 SPT boreholes collected in this geologic category was  
480 randomly selected. Then,  $T_{15,cs}$  was computed for the selected borehole according to Equation (3). Since  
481 each pixel was 30-m by 30-m, a semivariogram of  $T_{15,cs}$  was not utilized for developing weights during  
482 the random selection of the SPTs in a geologic unit. The semivariogram reached a sill at just 30 m which  
483 is identical to the spatial resolution of the maps; therefore, even it was used, it would have affected at  
484 most  $T_{15,cs}$  at four pixels per SPT.

485 To find  $T_{15,cs}$  for a given borehole required several additional nested steps because only saturated  
486 soils that are susceptible to liquefaction should be considered. In general, moderate to high plasticity  
487 clays are not considered susceptible to liquefaction (Boulangier and Idriss 2005; Bray and Sancio 2006),  
488 although some have exhibited softening behavior that is somewhat similar to liquefiable soils during  
489 major earthquakes. Saturated, coarse-grained, cohesionless soils with low fines contents are widely

490 considered susceptible to liquefaction. Clean sands are considered susceptible to liquefaction, and  
491 gravelly soils should be considered susceptible if they are bounded by materials with low permeability  
492 that allow build-up of excess pore-water pressure. It is much more difficult to define the susceptibility of  
493 soils with high fines contents (e.g., silty sands, clayey sands, sandy silts).

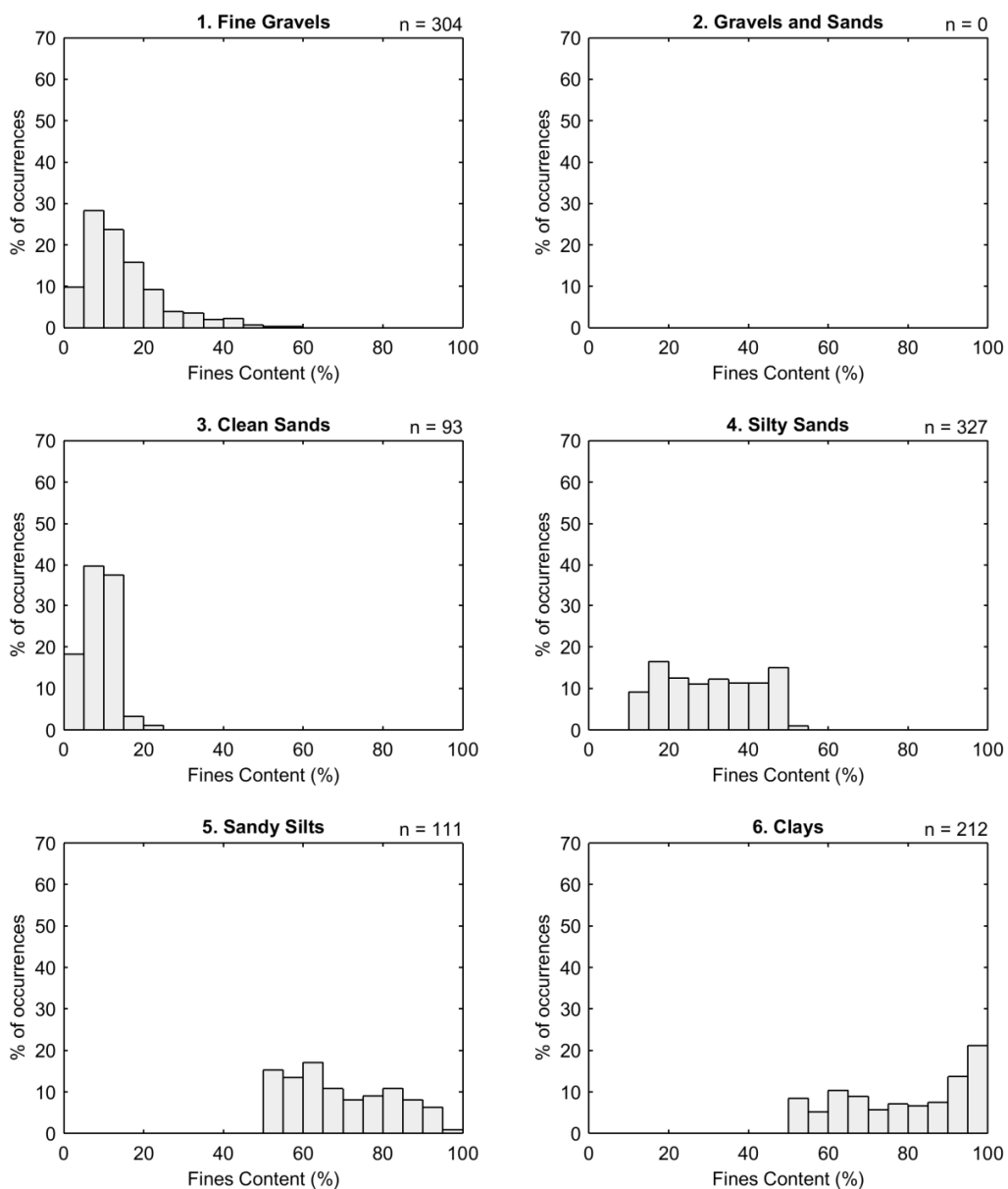
494 Boulanger and Idriss (2005) reviewed case histories and laboratory tests and identified two types of  
495 soil behavior on the basis of stress normalization and stress-strain response. Soils that exhibited *sand-like*  
496 behavior were considered susceptible to liquefaction, whereas soils that exhibited *clay-like* behavior were  
497 not considered susceptible. Boulanger and Idriss found that soil plasticity can be used to determine if the  
498 soil will exhibit sand-like or clay-like behavior, and proposed that the soil is clearly sand-like at a  
499 plasticity index ( $PI$ ) less than 3, and a soil is clearly clay-like at a  $PI$  greater than 8. Although they noted  
500 a transitional phase between 3 and 8, ultimately they recommended that engineers use a conservative  
501 guideline with  $PI = 7$  as the cutoff between sand-like and clay-like behavior when detailed laboratory  
502 testing is not possible. Thus, saturated soils with  $PI < 7$  should be considered susceptible to liquefaction,  
503 and only layers of soil with these characteristics were considered when computing  $T_{15,cs}$  at a selected  
504 borehole.

505 Unfortunately, values of  $PI$  as well as other soil properties were not reported for every layer of soil on  
506 the SPT logs in the geotechnical database. Thus, distributions of moisture contents, fines contents, and  
507 unit weights were developed using measurements recorded on *all* of the SPT logs in the database (i.e.,  
508 including the shallow logs). As expected, the distributions for these properties varied by soil type. Thus,  
509 for every layer on each SPT log, an  $SI$  value was first assigned per Table 1. Figure 4 shows one of the  
510 histograms of fines content, grouped according to  $SI$ . Refer to Gillins and Franke (2016) for other  
511 histograms of the dry unit weight, moisture content, and  $PI$  grouped by  $SI$  in Utah County. Nearly all of  
512 the soils with  $SI = 6$  had a  $PI > 7$ , and almost all of the silts, sandy silts, and silty sands (i.e.,  $SI = 4$  or  $5$ )  
513 had a  $PI < 7$  in the database.

514 Following recommendations in Boulanger and Idriss (2005), the authors first only considered the  
515 saturated layers of soil in the SPT log with  $PI < 7$  as susceptible to liquefaction when computing  $T_{15,cs}$ .



516 However, some of the layers in the log lacked Atterberg limits, unit weights, moisture contents, and fines  
 517 contents, all of which are necessary to correct raw SPT resistance ( $N_m$ ) to  $(N_1)_{60}$  to find  $T_{15,cs}$ . To  
 518 rigorously account for this uncertainty and continue with the Monte Carlo simulation, values for moisture  
 519 content, soil unit weight, and fines content were randomly sampled from the aforementioned distributions  
 520 according to the  $SI$  of any layer in the log which lacked these data.  
 521



523 **Figure 4.** Histograms for fines content for 6 different  $SI$  values, Utah County.

524

525 After simulating the missing data in the SPT log by random sampling for the  $i$ -th iteration of the  
526 Monte Carlo simulation,  $N_m$  was corrected to  $(N_1)_{60}$  as:

527 
$$(N_1)_{60} = C_E C_B C_R C_S C_N N_m \quad (12)$$

528

529 where  $C_E$  is the energy ratio correction factor accounting for the high variability in the amount of energy  
530 delivered to the drill rod stem by each impact of the SPT hammer,  $C_B$  is a correction factor for the  
531 borehole diameter,  $C_R$  is a correction factor for rod length,  $C_S$  is a correction factor for a sampler that had  
532 room for liners but was used without liners, and  $C_N$  is the overburden correction meant to account for the  
533 effects of increasing confining stress.

534 Recommended values and equations from Idriss and Boulanger (2008) were used for each of these  
535 SPT correction factors. Borehole diameters, rod lengths, and the use of liners were reported on the SPT  
536 logs for computing  $C_B$ ,  $C_R$ , and  $C_S$ , respectively. A value for  $C_N$  was computed for each simulation,  
537 because it is a function of the effective vertical stress and the soil stress profile varied slightly with each  
538 simulation according to the aforementioned randomly selected moisture contents and unit weights for  
539 those layers in the soil profile which lacked such data.

540 Many of the logs only reported the hammer release type (i.e., automatic or safety hammer) and did  
541 not include measurements of the energy delivered to the hammer for estimating  $C_E$ . Idriss and Boulanger  
542 (2008) report ranges of possible values for  $C_E$  according to the hammer type. For a safety hammer,  $C_E$  is  
543 reported to range from 0.7 to 1.2; for an automatic hammer, the range for  $C_E$  is reported as 0.8 to 1.3.  
544 (Note that none of the logs in the geotechnical database involved the use of a doughnut hammer.) It was  
545 assumed that these possible ranges for  $C_E$  are normally distributed, with a mean equal to the middle of the  
546 range, and a standard deviation equal to one-sixth of the range. Thus, for the  $i$ -th simulation, a value for  
547  $C_E$  was estimated ( $C_{E,i}$ ) as:

548 
$$C_{E,i} = \overline{C_E} + \sigma_{C_E} \cdot K_{rand,i} \quad (13)$$

549 where  $\overline{C_E}$  is a value of 1.0 or 1.1 for the safety hammer or automatic hammer, respectively,  $\sigma_{C_E}$  is a equal  
550 to 0.08 for both hammers, and  $K_{rand,i}$  is a random number generated for the simulation that follows the  
551 standard normal distribution.

552 After correcting  $(N_m)$  to  $(N_1)_{60}$  for the  $i$ -th simulation,  $T_{15,cs,i}$  for the  $i$ -th simulation was next  
553 found by computing the thickness of only those saturated layers of soil with a value of  $(N_1)_{60} < 15$  and  
554 with either: (1) a measured  $PI < 7$ , or (2) a value of  $SI \leq 5$  if the  $PI$  for the layer was not recorded on the  
555 log.

556 The computed values for  $T_{15,cs,i}$ ,  $W$ , and  $S$  (from the Step 1) were used with Equation (5) to compute  
557  $G_i$ . The regression coefficients for Equation (5) vary depending on the topography at the point of interest.  
558 For conservatism, Equation (5) was therefore solved twice—once for free-face conditions and once for  
559 ground-slope conditions. Then, the smaller of the two resulting values of  $G$  (i.e., the one that would  
560 produce the larger predicted lateral spread displacement) was assigned as  $G_i$  for the simulation.

561

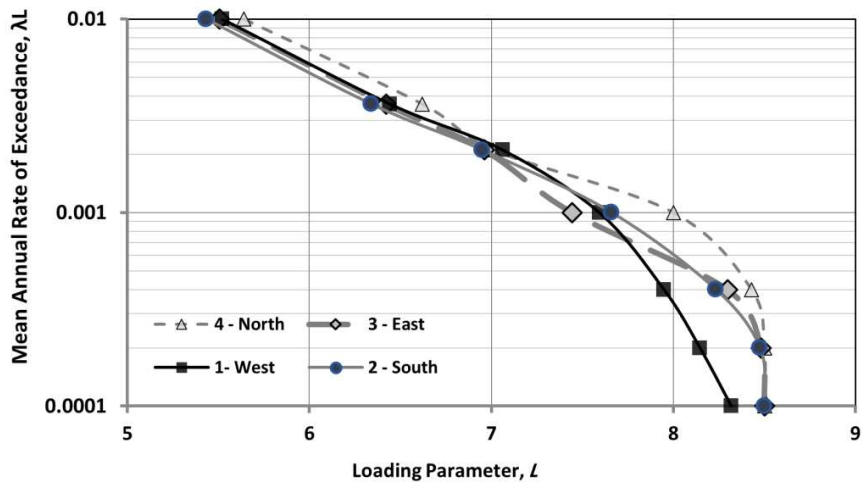
### 562 **Step 3: Input Seismic Loading**

563 Continuing with the  $i$ -th simulation, the next step was to randomly select and input an apparent loading  
564 value,  $\mathcal{L}_i$ , from the PDF of  $\mathcal{L}$  at the selected pixel. To develop the PDF, EZ-FRISK software (version  
565 7.62) was used to output hazard curves for  $\mathcal{L}$  from a PSHA at grid points evenly spaced every 0.05  
566 degrees in latitude and longitude (roughly every 3 to 5 km) across the study area. Franke (2005) outlined  
567 a procedure for programming EZ-FRISK to output an  $\mathcal{L}$  -hazard curve using its *Attenuation Table* feature.  
568 To use this table, values of  $\mathcal{L}$  were entered by solving Equation (4) at incremented values of  $M$  from 4.6  
569 to 8.4 (based on the normal crustal faults in Utah County, in increments of 0.2), and values of  $R$  of 1, 5,  
570 10, 15, 20, 25, 30, 40, 50, 60, 70, 80, 90, 100, 125, 150, 175, 200, 250, and 300 km. EZ-FRISK was set to  
571 use the USGS 2008 faults, areas, and background sources to perform the PSHAs (Peterson et al. 2008).

572 **The 2014 USGS models were not available in EZ-FRISK at the time of the study.** All USGS seismic

573 sources within 500 km of each grid point were included in the PSHAs, and hazard values for  $\mathcal{L}$  were  
574 output for return periods of 100, 275, 475, 1000, 2500, 5000, and 10000 years. Figure 5 presents  $\mathcal{L}$  -  
575 hazard curves at four grid points in the study area. The location of these four grid points is shown in  
576 Figure 6. Seven 30-m resolution raster images of  $\mathcal{L}$  for the above return periods were generated by  
577 bilinear interpolation of the  $\mathcal{L}$  -hazard curves computed at the evenly spaced grid points. Figure 6  
578 illustrates three of these raster images for  $\mathcal{L}$  at return periods of 1000, 2500, and 5000 years.

579 To perform the third step of the mapping process and continue with the  $i$ -th simulation, values for  $\mathcal{L}$   
580 were first extracted from each of the seven rasters at the selected pixel. This produced seven intermediate  
581 points on an  $\mathcal{L}$  -hazard curve at the pixel (similar to the points on the curves depicted in Figure 5). The  
582 points were then converted to units of return period so that an eighth intermediate point at (0,0) could be  
583 added. A linear interpolation (in increments of 0.1) between each of the eight intermediate points was  
584 then applied to the logarithm of the return period of the points, enabling production of numerous points  
585 along the  $\mathcal{L}$  -hazard curve at the mapping pixel. The exceedance probability for each of the points on the  
586 hazard curve was then computed using a Poisson probability distribution, and the results were binned into  
587 a PDF for binned values of  $\mathcal{L}$ . Next, a value for  $\mathcal{L}_i$  was randomly selected from the PDF for  $\mathcal{L}$  at the  
588 pixel.



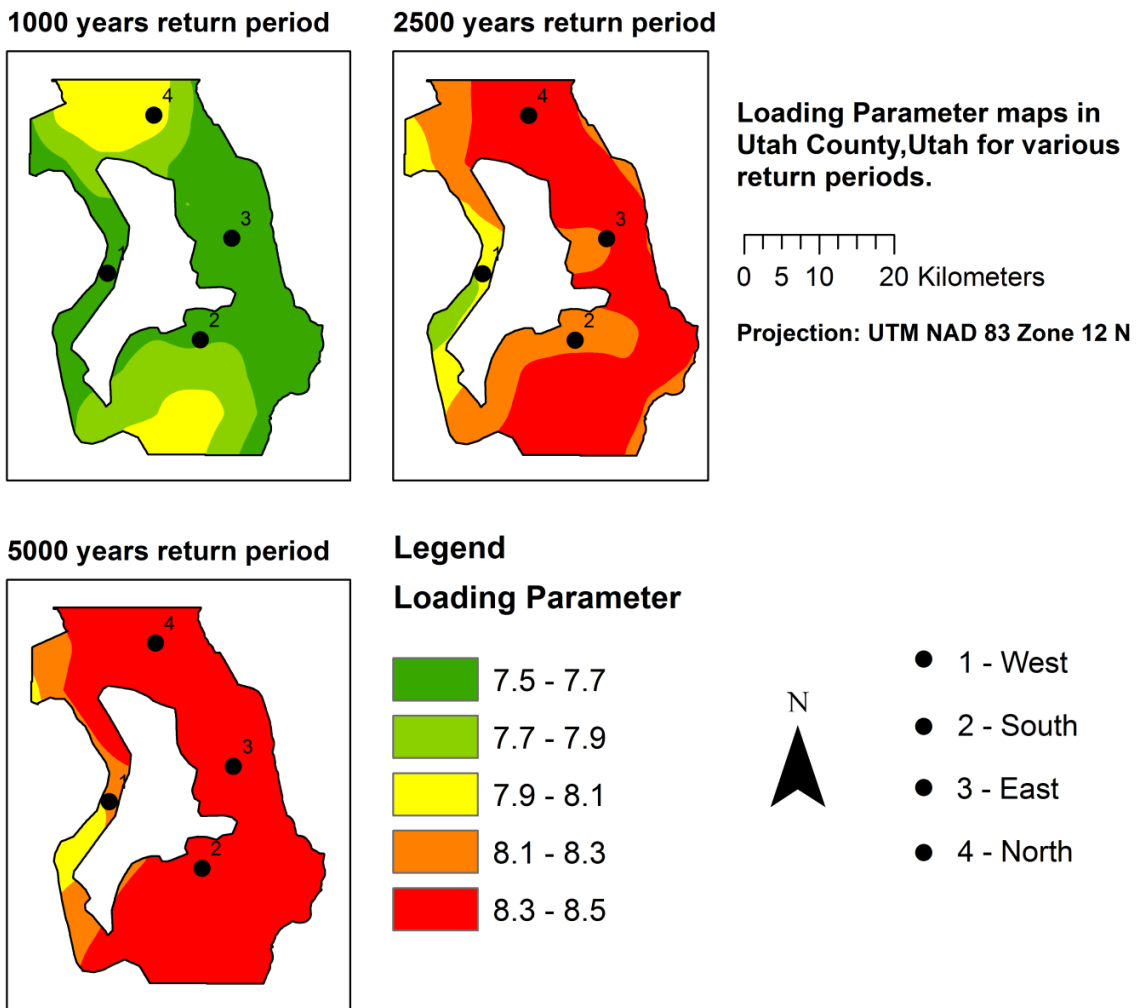
589

590

**Figure 5.** Apparent loading parameter hazard curves for four discrete locations in Utah County; which

591

are identified in Figure 6.



592

593

**Figure 6.** Apparent loading parameter hazard maps for a 1,000-year, 2,500-

594

year, and 5,000-year return period in Utah County.

595

**Step 4: Compute  $\log D_H$**

597

Continuing with the  $i$ -th simulation,  $G_i$  from Step 2 and  $\mathcal{L}_i$  from Step 3 were summed to find  $\overline{\log D_{Hi}}$ ,

598

then error in the lateral spread displacement model was simulated by solving Eq. 10 in order to output a

599

value for  $[\log D_H]_i$ .

600

601 **Step 5: Repeat Steps 2 – 4, Produce  $D_H$  Distribution**

602 Numerous simulations are necessary to model the several sources of uncertainty in the subsurface  
603 characterization (i.e.,  $(N_1)_{60}$ ,  $T_{15,CS}$ ,  $C_E$ ), seismic hazard (i.e.,  $\mathcal{L}$ ), and lateral spread displacement  
604 modeling error (i.e.,  $\epsilon$ ). As further discussed below, Steps 2 – 4 were repeated 200,000 times for each  
605 pixel, resulting in a distribution of  $\log D_H$  values at each pixel. This distribution was then converted into  
606 a distribution of  $D_H$  values (in meters). Note a new SPT for a given geologic unit was randomly selected  
607 for each simulation with replacement.

608

609 **Step 6: Compute  $D_H$  Hazard Curve**

610 The next step in the mapping procedure was to convert the 200,000  $D_H$  values at a pixel from the  
611 Monte Carlo simulations into a  $D_H$ -hazard curve. To make this conversion, the distribution for  $D_H$  was  
612 first converted into an empirical cumulative distribution function (CDF) curve. The annual probability  
613 that  $D_H$  exceeds a displacement value,  $d$ , of interest (i.e.,  $P(D_H > d)$ ) is equal to *1 minus the CDF* value at  $d$   
614 on this curve. (Note that the CDF is always equal to the non-exceedance probability; therefore, in this  
615 case, the CDF equals the probability  $D_H$  does not exceed  $d$ ). The annual exceedance probability was  
616 defined using the Poisson model (Eq. 11), where  $t = 1$  year for an annual probability, and  $\lambda =$  the mean  
617 annual rate of exceedance.

618 Table 4 lists some typical return periods of interest and their corresponding values of  $\lambda$ , annual  
619 exceedance probability, and CDF. Using the empirical CDF, points on the  $D_H$ -hazard curve at a selected  
620 pixel were developed by finding the displacement value at each of the CDF values listed in Table 4. As  
621 an example, the fifth column of Table 4 presents a set of displacement values taken from an empirical  
622 CDF at a particular pixel in the study area. Plotting  $\lambda$  versus  $d$  from Table 4, the  $D_H$ -hazard curve for this  
623 example set of data can be depicted, as shown in Figure 7a.

624 It is interesting to consider the meaning of the hazard curve depicted in Figure 7a and tabulated in  
625 Table 4. For a 475-year or 2,475-year return period hazard, the annual exceedance probability equals  
626 only 0.2% and 0.04%, respectively. Clearly, for a given year, these extreme hazard levels are highly

627 unlikely; nonetheless, engineers are concerned with such hazard levels because the extreme events can  
 628 cause significant damage. Upon further inspection of the example data in Table 4, 0.2% (or 400 of the  
 629 200,000 simulations) of the data in the  $D_H$  distribution at the mapping pixel exceeded a displacement  
 630 value of 0.01 m, and only 0.04% (or 80 of the 200,000 simulations) exceeded a displacement value of  
 631 0.43 m. These lateral spread displacement values of 0.01 m and 0.43 m therefore correspond to the 475-  
 632 year and 2475-year return period hazards, respectively.

633 Since the extreme values in the  $D_H$  distributions are of greatest interest when mapping the lateral  
 634 spread hazard, it is important to perform many Monte Carlo simulations. In addition, numerous  
 635 simulations ensure that the uncertainties in the mapping process are modeled well. The authors decided  
 636 to run 200,000 simulations for each pixel. This large number was selected because it produced a  $D_H$ -  
 637 hazard curve that looked similar to a  $D_H$ -hazard curve after 300,000 or 400,000 simulations at return  
 638 periods less than 2475 years, and it did not overburden the computer with excessive computational time.  
 639 For example, Figure 7b presents  $D_H$ -hazard curves at the same mapping pixel after running 10000, 50000,  
 640 100000, 200000, 300000, and 400000 simulations. The curve for 10000 simulations appears different  
 641 than the other curves, and the authors concluded after several tests at numerous pixels that this number of  
 642 simulations was inadequate. The curves appear fairly similar when  $N \geq 100000$  simulations, especially  
 643 at return periods less than 2475 years (i.e.,  $\lambda < 0.0004$ ).

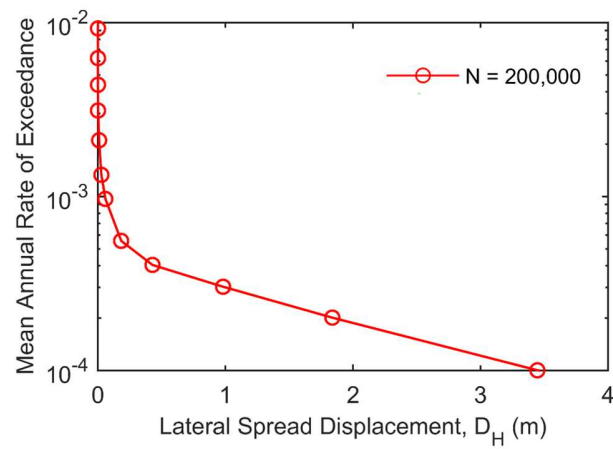
644

645 **Table 4.** Example distribution of  $D_H$  values at listed return periods

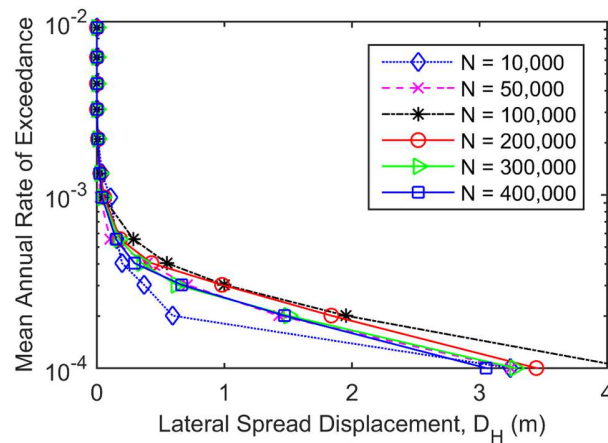
Return Period [ $1/\lambda$ ] (years)	Mean annual rate of exceedance, $\lambda$	Annual Exceedance Probability [ $P(D_H > d)$ ]	CDF [ $P(D_H < d)$ ]	$d$ (meters)
108	0.01	0.009	0.991	0.00
228	0.004	0.0044	0.9956	0.00
475	0.002	0.0021	0.9979	0.01
1033	0.001	0.0010	0.9990	0.06
2475	0.0004	0.00040	0.99960	0.43
4975	0.0002	0.00020	0.99980	1.84
9975	0.0001	0.00010	0.99990	3.45

646





(a)



(b)

648

649 **Figure 7.** (a) Example  $D_H$ -hazard curve at a mapping pixel after 200,000 Monte Carlo simulations; (b) a650 set of  $D_H$ -hazard curves at the same mapping pixel after different numbers of Monte Carlo simulations.

651

652 **Step 7: Repeat Steps 1-6 for All Map Pixels**

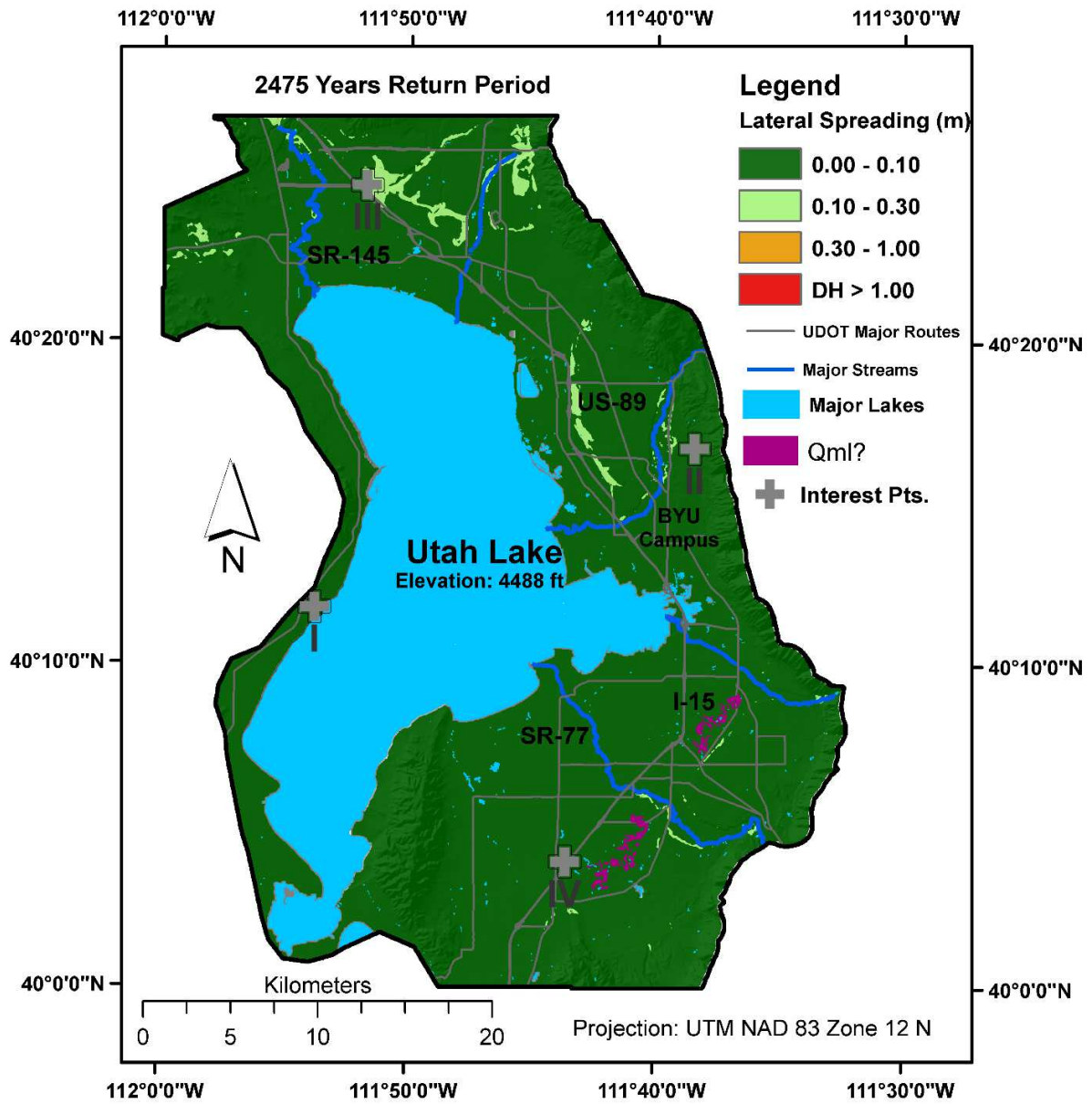
653 The first six steps of the mapping procedure were repeated for every pixel in the study area. Upon

654 completion, a  $D_H$ -hazard curve similar to the one depicted in Figure 7a was generated for every pixel.

655

656 **Step 8: Output  $D_H$  Hazard Map**

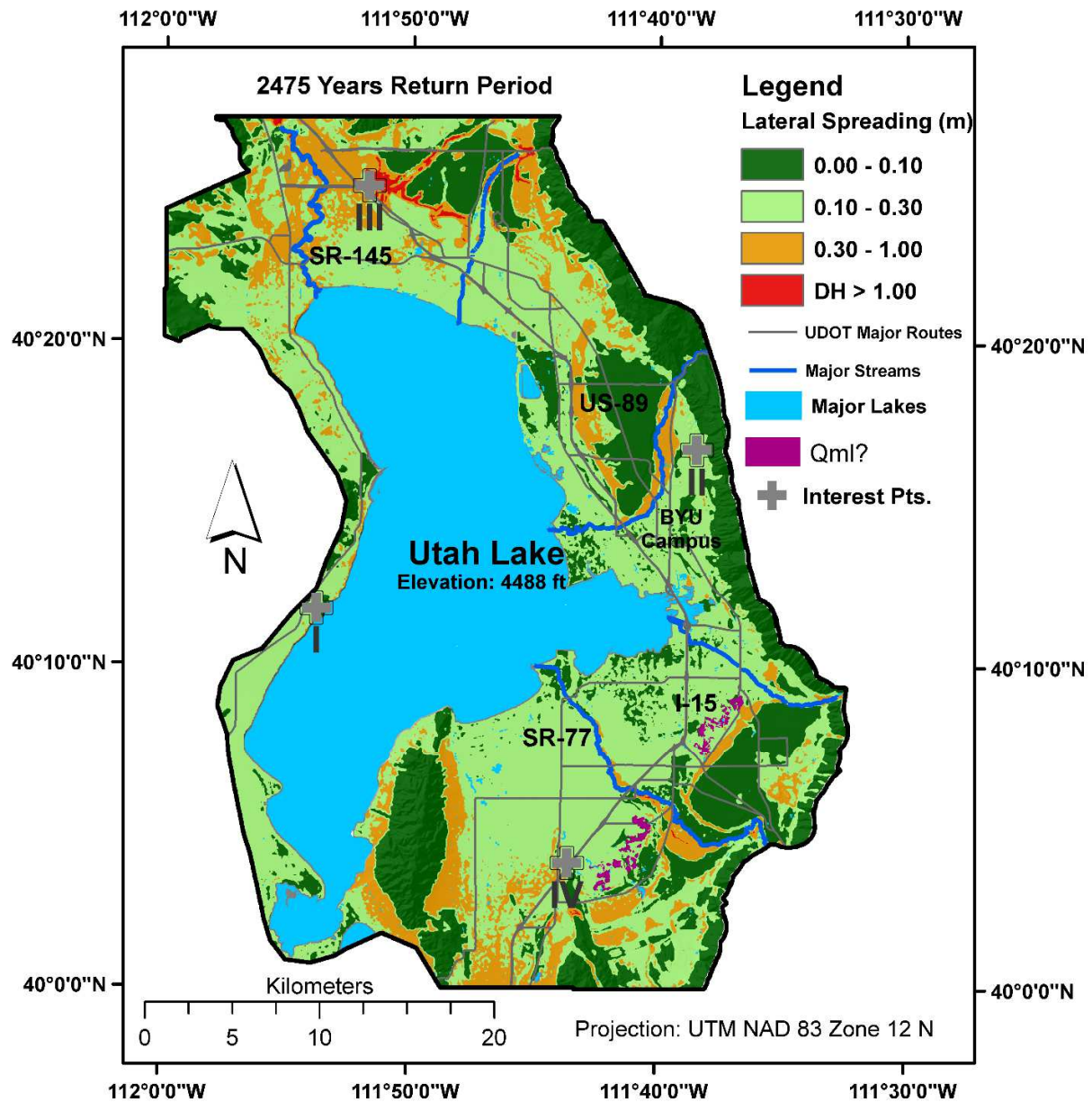
657 The final step was to produce 30-m resolution raster hazard maps at the desired return periods. This  
658 was performed by simply extracting the  $D_H$  value from the  $D_H$ -hazard curve at a desired return period  
659 (e.g., 475, 1,33, or 2475-year return period) for each pixel, and then storing the extracted data as raster  
660 values in a raster image of the study area. Because the  $D_H$ -hazard curves were already computed at a  
661 resolution of 30-m for the study area, no additional interpolation was necessary. The raster images for  
662 return periods of 1033, and 2475 years were visualized in GIS to produce the final hazard maps (Figures 8  
663 and 9).



664

665

**Figure 8.** The 1,033-year return period lateral spread hazard map, Utah County, Utah.



666

667 **Figure 9.** The 2,475-year return period lateral spread displacement hazard map, Utah County, Utah.

668

669 **7. RESULTS AND DISCUSSION**

670 The Anderson et al. (1994) map (Figure 2) indicates that a significant portion of the study area has

671 *high* liquefaction potential. **However, this map does not give any indication of the severity of ground**

672 failures nor does it show possible consequences like lateral spread. Mapping lateral spread displacements  
673 such as those in Figures 8 and 9 is advantageous because large displacements are strongly correlated with  
674 potential damage.

675 Figure 8 shows that lateral spread displacements are not generally expected to exceed 0.1 m for  
676 almost the entire study area at a return period of 1,033 years. Nevertheless, the map does show some  
677 displacements may reach up to 0.3 m in some of the lacustrine sand and young alluvial fan units with  
678 sufficient topographic relief (i.e., near a free-face or on sloping ground). Except for these relatively small  
679 locales, it is concluded that the lateral spread hazard is minimal at the 1,033-year return period in most of  
680 the study area. This finding highlights one of the benefits of producing fully-probabilistic hazard maps.  
681 Some building codes require design engineers to evaluate structures, foundations, and lifelines to  
682 withstand a 475-year or 1033-year return period hazard. Our results at this return period indicate that the  
683 potential for significant lateral spread displacement and damage are very localized.

684 However, for critical infrastructure, building codes may require engineers to evaluate the hazard for  
685 less frequent events (i.e., lower probability of non-exceedance). Based on our mapping efforts, we  
686 conclude that some locations in the study area may experience significant lateral spread displacements at  
687 the 2475-year return period hazard level. Figure 9 shows limited portions of the study area that may  
688 undergo displacements greater than 1 m and some areas may experience displacements exceeding 0.3m.  
689 In short locales having the combined characteristics of liquefiable layers with sufficient  $T_{15,cs}$  values,  
690 topographic relief, and apparent seismic loading may undergo damaging horizontal displacement during  
691 major, nearby earthquakes. Notwithstanding, even though the map does suggest the potential for  
692 significant lateral spread hazard in localized areas, the majority of the map generally shows displacements  
693 less than 0.3 m.

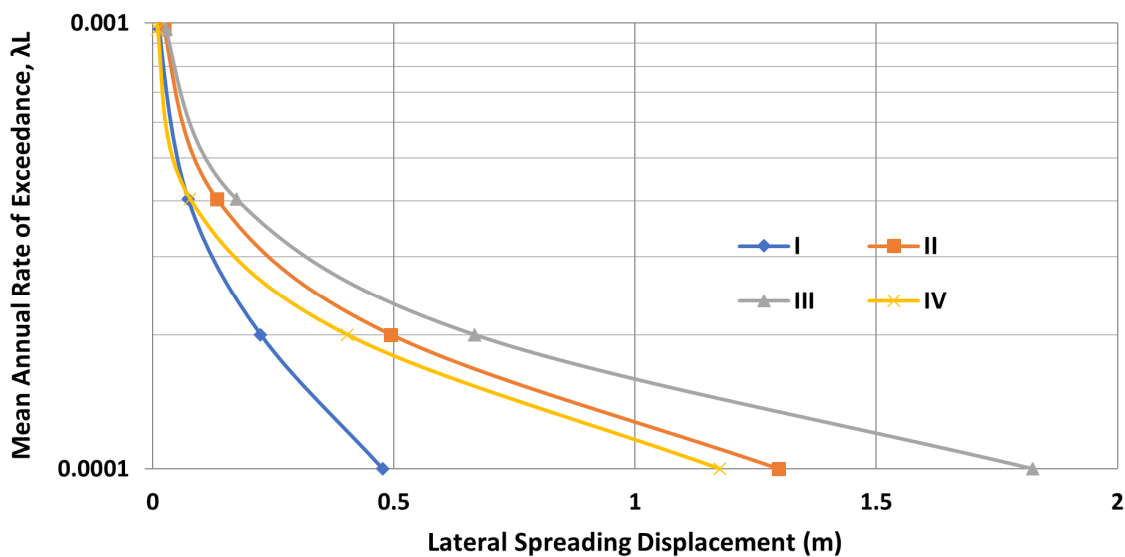
694 In additional evaluations, it was found that when simulating a major earthquake (i.e., large value for  
695  $\mathcal{L}$ ) as a result of fault rupture of the nearby Utah segment of the Wasatch Fault Zone, the relatively high

696 estimated strong motion and its close proximity to the study area frequently produced at least small  $D_H$   
697 values ranging from 0.1 to 0.3 m in geologic units with nonzero  $T_{15,CS}$  values.

698 Figure 10 presents  $D_H$ -hazard curves at 4 points of interest, as located in Figures 8 and 9. The Figure  
699 highlights how the displacement hazard varies in the study area. For example, Point III is near the I-15  
700 corridor, north of Utah Lake. The lateral spread displacement hazard was greatest at this point as  
701 compared with the other points. Point I is west of Utah Lake and has the lowest displacement hazard as  
702 compared with the other points. This is likely because Point I has a lower apparent loading hazard as it is  
703 further from the Wasatch Fault Zone.

704 It is worth noting that the geologic map for Utah County (Figure 3) identifies some small deposits  
705 east of the I-15 corridor and southeasterly of Utah Lake which may have underwent lateral spreading  
706 during a prehistoric earthquake. These deposits were labeled as “*Qml? Lateral-spread deposits?*” on the  
707 Constenius et al. (2011) map. Unfortunately, none of the available investigations in the geotechnical  
708 database were within these deposits. Given that they may have underwent lateral spreading in the past,  
709 and because of a lack of geotechnical data in these deposits, these areas were hatched in hazard maps in  
710 Figures 8 and 9. Further research is needed to determine the lateral spread hazard for the *Qml?* unit.

711



712

713 **Figure 10.** Lateral spreading displacement hazard curves for 4 points of interest in the study area.

## 714 **8. CONCLUSIONS**

715 This paper proposed methods to develop fully probabilistic lateral spread displacement hazard maps  
716 using available seismic, geotechnical, geological and topographical data. These methods were then  
717 implemented to produce hazard maps at return periods of 1033 and 2475 years for Utah County, Utah.  
718 Although the paper focused on this county, other areas could also be mapped following similar  
719 procedures.

720 The lateral spread displacement map show a negligible displacement hazard at a return period of 1033  
721 years. However, at the more extreme 2475-year return period, estimated displacements may exceed 1 m  
722 in a few locations in the study area. This is because: (1) numerous SPT borehole logs in the geotechnical  
723 database show layers of loosely deposited, cohesionless soils; (2) a significant portion of the area has a  
724 shallow groundwater table due to its proximity to Utah Lake; and (3) the area is in very close proximity to  
725 the Utah segment of the Wasatch Fault Zone which is capable of generating a major earthquake with  $M_w$   
726  $\geq 7$ . Clearly, liquefaction and its effects should be a major concern for Utah County as well as other parts  
727 of the Wasatch Front. It is recommended to conduct additional site-specific studies at areas with high  
728 lateral spread hazard.

729 The methods presented in this paper are new and innovative. First, the hazard maps are based on  
730 seismic loading from a fully probabilistic seismic hazard analysis (PSHA). Previous liquefaction hazard  
731 mapping efforts (e.g., Anderson et al. 1982; Bartlett et al. 2005; Baise et al. 2006; Holzer et al. 2006;  
732 Olsen et al. 2007; Gillins 2012) show hazard levels given either a constant peak ground acceleration for  
733 the entire study area, a deterministic scenario event, or an event from a single return period of the  
734 deaggregation of a probabilistic seismic hazard analysis. Second, using Monte Carlo random sampling  
735 techniques, the maps presented in this paper modeled the uncertainty in the in state-of-the-art lateral  
736 spread displacement (i.e., Gillins and Bartlett 2013) empirical equation by using its published standard  
737 deviation per Eq. 10. Lastly, the lateral spread hazard maps modeled the spatial variation in ground slopes  
738 and free faces using a highly-resolute DEM developed from aerial lidar data collected in 2013.

739 The maps are intended to convey preliminary hazard information to city planners, developers, and  
740 engineers. Because mapping liquefaction and ground displacement hazards for a regional area is  
741 challenging, the authors recognize some parts of the maps have large uncertainty, and perhaps errors  
742 associated with the data. Although the maps are based on over 750 geotechnical boreholes, significant  
743 uncertainties remain in the subsurface conditions. For example, the authors noticed marked variability in  
744 the results of SPT investigations—even for those found in the same geologic unit and located within 100  
745 m of each other. The authors attempted to account for this variability while mapping Utah County by  
746 developing distributions of geotechnical properties using tens to hundreds of available SPT boreholes  
747 found in each geologic unit. However, it is inappropriate to assume that a few local SPT investigations at  
748 a discrete location fully characterizes the uncertainties in subsurface conditions for an entire, widespread  
749 geologic unit. Therefore, it is hoped that practicing professionals will continue performing site-specific  
750 evaluations, especially in areas mapped with high lateral spread displacement hazard in order to refine the  
751 mapped estimates. Furthermore, by conducting and compiling additional investigations, it would be  
752 possible to update and improve the maps as the dataset and knowledge evolve. For example, the maps  
753 could be updated when new earthquake models or strong motion estimates are published by the USGS, or  
754 as new or revised lateral spread displacement models become available.

755 Although the mapping methodology discussed herein should be considered a step forward from  
756 previous hazard mapping efforts, the presented maps are still not intended nor recommended for site-  
757 specific engineering evaluations and design. The authors strongly encourage individuals engaged in  
758 evaluating, designing, building, or maintaining infrastructure— especially critical infrastructure—to  
759 continue performing site-specific liquefaction hazard evaluations using qualified experts. Experienced  
760 professionals should be consulted regarding their knowledge of the study area based on prior geologic  
761 mapping and geotechnical investigative efforts. Such experts may be able to note discrete areas on the  
762 hazard maps that are inconsistent with their knowledge and experience of the conditions at specific  
763 locales.



764 More site-specific testing will be invaluable and the new geotechnical investigations could be added  
765 to the geotechnical database in order to improve the characterization of the subsurface. The maps  
766 presented herein for Utah County are based on available SPTs collected in a non-systematic manner over  
767 multiple decades. A higher density of geotechnical investigations distributed more thoroughly across the  
768 study area could be used to improve the accuracy of the maps presented in this paper. With more SPTs, it  
769 may be possible to spatially interpolate  $T_{15,cs}$  through the SPT locations using some type of geostatistical  
770 method, such as has been done for other study areas (e.g., Liu et al. 2016; Juang et al. 2017; Baker et al.  
771 2008; Chen et al. 2016), than estimating  $T_{15,cs}$  from sets of SPTs for each geologic unit. Moreover, it  
772 could allow development of a realistic ground water table model and possibly a reliable 3D subsurface  
773 model for future hazard mapping.

774

775

## 9. ACKNOWLEDGEMENTS

776 This research was supported by the U.S. Geological Survey (USGS), Department of the Interior,  
777 under USGS award numbers G14AP00118 and G14AP00119, as well as by the Utah Department of  
778 Transportation and the Central Utah and Weber Basin Water Conservancy Districts. The views and  
779 conclusions contained in this document are those of the authors and should not be interpreted as  
780 necessarily representing the official policies, either expressed or implied, of these government agencies.

781

782

## 10. REFERENCES

783 Anderson, L.R., Keaton, J.R., Aubrey, Kevin, and Ellis, S.J. (1982). "Liquefaction Potential Map for  
784 Davis County, Utah," Logan, Utah State University Department of Civil and Environmental  
785 Engineering and Dames and Moore unpublished Final Technical Report prepared for the U.S.  
786 Geological Survey, National Earthquake Hazards Reduction Program Award No. 14-08-0001-19127,  
787 50 p.; published as Utah Geological Survey Contract Report 94-7, 1994.

788 Anderson, L.R., Keaton, J.R., and Bischoff, J.E. (1994a). "Liquefaction Potential Map for Utah County,  
789 Utah," Logan, Utah State University Department of Civil and Environmental Engineering and Dames  
790 and Moore unpublished Final Technical Report prepared for the U.S. Geological Survey, National  
791 Earthquake Hazards Reduction Program Award No. 14-08-0001-21359, 46 p., 1986; published as  
792 Utah Geological Survey Contract Report 94-8, 1994.

- 793 Anderson, L.R., Keaton, J.R., and Eldredge, S.N. (1994b). Liquefaction-potential map for a part of Utah  
794 County, Utah: Utah Geological Survey Public Information Series 28, 2 p., scale 1:365,000, accessed  
795 online June 6, 2017 at [http://ugspub.nr.utah.gov/publications/public\\_information/pi-28.pdf](http://ugspub.nr.utah.gov/publications/public_information/pi-28.pdf).
- 796 Automated Geographic Reference Center (AGRC). (2014), Wasatch Front lidar, State of Utah, acquired  
797 from <http://gis.utah.gov/data/elevation-terrain-data/2013-2014-lidar/>.
- 798 Baise, L.G., Higgins, R.B., and Brankman, C.M. (2006). "Liquefaction Hazard Mapping – Statistical and  
799 Spatial Characterization of Susceptible Units." *J. Geotech. & Geoenviron. Eng.*, Vol. 132, No. 6, 705-  
800 715.
- 801 Baker, J. W., & Faber, M. H. (2008). Liquefaction risk assessment using geostatistics to account for soil  
802 spatial variability. *Journal of geotechnical and geoenvironmental engineering*, 134(1), 14-23.
- 803 Bardet, J.P., Tobita, T., Mace, N., and Hu, J. (2002). "Regional Modeling of Liquefaction-Induced  
804 Ground Deformation", *Earthquake Spectra*, 18(1), 19-46.
- 805 Bartlett S. F., Olsen, M. J., and Solomon, B. J. (2005). "Lateral Spread Hazard Mapping of Northern Salt  
806 Lake County for a Magnitude 7.0 Scenario Earthquake," Technical Report submitted to the United  
807 States Geological Survey, NERHP Award No. 04HQGR0026, 218 p.
- 808 Bartlett, S.F., and Youd, T.L. (1995). "Empirical prediction of liquefaction-induced lateral spread." *J.*  
809 *Geotech. Eng.*, 121(4), 316-329.
- 810 Bazzurro, P., and Cornell, C. A. (2004). "Nonlinear soil-site effects in probabilistic seismic-hazard  
811 analysis." *Bulletin of the Seismological Society of America*, 94(6), 2110-2123.
- 812 Boulanger, R.W., and Idriss, I.M. (2005). "Evaluating cyclic failure in silts and clays," *Proc. of*  
813 *Geotechnical Earthquake Engrg. Satellite Conf. on Performance-Based Design in Earthquake*  
814 *Geotech. Engrg: Concepts and Research*. Prepared by TC4 Committee of ICSMGE, Japanese  
815 Geotechnical Society, Tokyo, 78-86.
- 816 Bray, J. D., and Sancio, R. B. (2006). "Assessment of the liquefaction susceptibility of fine-grained  
817 soils." *J. Geotech. Geoenviron. Eng.*, 132(9), 1165-1177.
- 818 Bray, J. D., and Travasarou, T. (2007). "Simplified procedure for estimating earthquake-induced  
819 deviatoric slope displacements." *J. Geotech. Geoenviron. Eng.*, 133(4), 381–392.
- 820 Chen, Q., Wang, C., & Juang, C. H. (2016). Probabilistic and spatial assessment of liquefaction-induced  
821 settlements through multiscale random field models. *Engineering Geology*, 211, 135-149.
- 822 Constenius, K.N., Clark, D.L., King, J.K., and Buck Ehler, J. (2011). "Interim Geologic Map of the Provo  
823 30' x 60' Quadrangle, Utah, Wasatch, and Salt Lake Counties, Utah," *Open-File Report 586DM*,  
824 Utah Geological Survey.

- 825 Cornell, C. A., and Krawinkler, H. (2000). "Progress and challenges in seismic performance assessment."  
826 PEER Center News, 3(2), 1–4.
- 827 Cramer, C. H., Rix, G. J., and Tucker, K. (2008). "Probabilistic liquefaction hazard maps for Memphis,  
828 Tennessee." *Seismological Research Letters*, 79(3), 416-423.
- 829
- 830 Deierlein, G. G., Krawinkler, H., and Cornell, C. A. (2003). "A framework for performance-based  
831 earthquake engineering." *Proc., 2003 Pacific Conf. on Earthquake Engineering*.
- 832 Erickson, G. L. (2006) "Probabilistic liquefaction potential mapping of the Salt Lake Valley" M.S Thesis,  
833 Univ. of Utah, Salt Lake City.
- 834 EZ-FRISK 7.60 [Computer software]. Boulder, CO, Risk Engineering
- 835 Faris, A.T., Seed, R.B., Kayen, R.E., and Wu, J. (2006). "A semi-empirical model for the estimation of  
836 maximum horizontal displacement due to liquefaction-induced lateral spreading." Vol. 3, *Proc., 8<sup>th</sup>*  
837 *U.S. Nat. Conf. Earthquake Engrg.*, Earthquake Engineering Research Institute, Oakland, CA, 1584-  
838 1583.
- 839 Franke, K.W. (2005). "Development of a performance-based model for the prediction of lateral spreading  
840 displacements." M.S. thesis, Univ. of Washington, Seattle.
- 841 Franke, K.W. and Kramer, S.L. (2014). "Procedure for the Empirical Evaluation of Lateral Spread  
842 Displacement Hazard Curves." *J. Geotech. & Geoenviron. Eng.*, 140(1), 2014.140:110-120.
- 843 Gillins, D.T. (2012). "Mapping the Probability and Uncertainty of Liquefaction-Induced Ground Failure"  
844 Ph.D. Dissertation, Univ. of Utah, Salt Lake City.
- 845 Gillins, D.T. (2014). "Considering Topography when Mapping Liquefaction Hazard with the  
846 Liquefaction Potential Index," *Proc. 10<sup>th</sup> National Conf. on Earthquake Engrg.*, Anchorage, Alaska,  
847 July 21-25, 12 pp.
- 848 Gillins, D.T. and Bartlett, S.F. (2013). "Multilinear Regression Equations for Predicting Lateral Spread  
849 Displacement from Soil Type and Cone Penetration Test Data." *J. Geotech. & Geoenviron. Eng.*,  
850 140(4), 04013047.
- 851 Gillins, D.T., and Franke, K. (2016). "Probabilistic Liquefaction Potential and Lateral Spread Hazard  
852 Maps for Utah County, Utah: Collaborative Research with Brigham Young University and Oregon  
853 State University", *USGS External Research Report*, USGS Award Nos. G14AP00118 and  
854 G14AP00119, Reston, VA, 89 pp.
- 855 Hamada, M., Yasuda, S., Isoyama, R., and Emoto, K. (1986). "Study on liquefaction induced permanent  
856 ground displacements." *Report for the Association for the Development of Earthquake Prediction in*  
857 *Japan*, Tokyo, Japan, 87 pp.

- 858 Holzer, T.L., Blair, J.L., Noce, T.E., and Bennett, M.J. (2006). "LiqueMap: A Real-Time Post Earthquake  
859 Map of Liquefaction Probability." Proc., 8th US National Conference on Earthquake Eng., EERI,  
860 Oakland, CA.
- 861 Idriss, I.M., and Boulanger, R.W. (2008). *Soil liquefaction during earthquakes*, Earthquake Engineering  
862 Research Institute Monograph MNO-12, Earthquake Engineering Research Institute, Oakland, CA,  
863 262 pp.
- 864 Idriss, I. M., and Boulanger, R. W. (2012). "Examination of SPT-based liquefaction triggering  
865 correlations." *Earthquake Spectra*, 28(3), 989-1018.
- 866 Iwasaki, T., Tokida, K., Tatsuoka, F., Watanabe, S., Yasuda, S., and Sato, H. (1982). "Microzonation for  
867 soil liquefaction potential using simplified methods." In Proceedings of the 3rd international  
868 conference on microzonation, Seattle, Vol. 3, pp. 1310-1330.
- 869 Jaimes, M. A., Niño, M., & Reinoso, E. (2015). "Regional map of earthquake-induced liquefaction hazard  
870 using the lateral spreading displacement index D<sub>LL</sub>." *Natural Hazards*, 77(3), 1595-1618.
- 871 Juang C H, Shen M, Wang C. et al. (2017). "Random field-based regional liquefaction hazard mapping —  
872 data inference and model verification using a synthetic digital soil field". *Bull Eng Geol Environ*.  
873 <https://doi.org/10.1007/s10064-017-1071-y>
- 874 Lam, I., Arduino, P., and Mackenzie-Helnwein, P. (2009). "OpenSees soilpile interaction study under  
875 lateral spread loading." *Int. Foundation Congress & Equipment Expo '09*, ASCE, Reston, VA, 206–  
876 213.
- 877 Lee, D. H., Ku, C. S., and Yuan, H. (2004). "A study of the liquefaction risk potential at Yuanlin,  
878 Taiwan." *Engineering Geology*, 71(1), 97-117.
- 879 Lenz, J. A., and Baise, L. G. (2007). "Spatial variability of liquefaction potential in regional mapping  
880 using CPT and SPT data." *Soil Dynamics and Earthquake Engineering*, 27(7), 690-702.
- 881 Liu, F., Li, Z., Jiang, M., Frattini, P., & Crosta, G. (2016). Quantitative liquefaction-induced lateral  
882 spread hazard mapping. *Engineering Geology*, 207, 36-47.
- 883 Luna, R., and Frost, J. D. (1998). "Spatial liquefaction analysis system." *Journal of Computing in Civil  
884 Engineering*, 12(1), 48-56.
- 885 Mabey, M. A., and Madin, I. (1993). *Relative Earthquake Hazard Map: Portland, Oregon 7-1/2 Minute  
886 Quadrangle*. Oregon Department of Geology and Mineral Industries.
- 887 Maurer, B. W., Green, R. A., Cubrinovski, M., and Bradley, B. A. (2014). "Evaluation of the  
888 Liquefaction Potential Index for Assessing Liquefaction Hazard in Christchurch, New Zealand."  
889 *Journal of Geotechnical and Geoenvironmental Engineering*, 140(7), 04014032.

- 890 National Research Council (NRC) (1985). Liquefaction of Soils During Earthquakes, National Academy  
891 Press, Washington D.C., 240 p.
- 892 Olsen, M. J., Bartlett, S. F., and Solomon, B. J., (2007). “Lateral Spread Hazard Mapping of the Northern  
893 Salt Lake Valley, Utah, for M7.0 Scenario Earthquake,” *Earthquake Spectra*, 23(1), 95-113.
- 894 Petersen, M. D., Frankel, A. D., Harmsen, S. C., Mueller, C. S., Haller, K. M., Wheeler, R. L., Wesson,  
895 R.L., Zeng, Y., Boyd, O.S., Perkins, D.M. and Luco, N. (2008). Documentation for the 2008 update  
896 of the United States national seismic hazard maps (No. 2008-1128). Geological Survey (US).
- 897 Rashidian, V., and Gillins, D.T. (2018). “Modification of the Liquefaction Potential Index to Consider the  
898 Topography in Christchurch, New Zealand,” *Engineering Geology*, 232, 68-81.
- 899 Rauch, A.F., and Martin, J.R. (2000). “EPOLLS Model for Predicting Average Displacements on Lateral  
900 Spreads”, *J. Geotech. & Geoenviron. Eng.*, ASCE, 126(4), 360-371.
- 901 Saygili, G., and Rathje, E. M. (2008). Empirical predictive models for earthquake-induced sliding  
902 displacements of slopes. *J. Geotech. Geoenviron. Eng.*, 134(6), 790–803.
- 903 Seed, H.B. (1979). “Soil liquefaction and cyclic mobility evaluation for level ground during earthquakes,”  
904 *Journal of Geotechnical Engineering Div.* 105(2), 201-255.
- 905 Seid-Karbasi, M., and Byrne, P. M. (2007). “Seismic liquefaction, lateral spreading and flow slides: A  
906 numerical investigation into void redistribution.” *Can. Geotech. J.*, 44(7), 873–890.
- 907 Sharifi-Mood, M. (2017). “Probabilistic Geospatial Analyses, Uncertainty Modeling, and Mapping of  
908 Seismically-induced Ground Failures” Ph.D. Dissertation, Oregon State University, Corvallis,  
909 [http://ir.library.oregonstate.edu/concern/graduate\\_thesis\\_or\\_dissertations/x059cd09j](http://ir.library.oregonstate.edu/concern/graduate_thesis_or_dissertations/x059cd09j)
- 910 Sonmez, H., and Gokceoglu, C. (2005). “A liquefaction severity index suggested for engineering  
911 practice.” *Environmental Geology*, 48(1), 81-91.
- 912 Stewart, J. P., Afshari, K., & Hashash, Y. M. (2014). “Guidelines for performing hazard-consistent one-  
913 dimensional ground response analysis for ground motion prediction.” PEER Report 2014/16, Pacific  
914 Earthquake Engineering Research Center, Berkeley, CA.
- 915 Ulmer, K., Ekstrom, L., & Franke, K. (2015). “Optimum Grid Spacing for Simplified Performance-based  
916 Liquefaction and Lateral Spread Displacement Parameter Maps.” Proc. 6th International Conference  
917 on Earthquake Geotechnical Engineering, Nov 1. Christchurch, New Zealand.
- 918 Youd, T. L., and Hoose, S. N. (1977). “Liquefaction susceptibility and geologic setting.” In Proc., 6th  
919 World Conf. on Earthquake Engineering, Vol. 6, pp. 37-42. Roorkee, India: Indian Society of  
920 Earthquake Technology.
- 921 Youd, T. L., Hansen, C. M., and Bartlett S. F. (2002). “Revised multilinear regression equations for  
922 prediction of lateral spread displacement.” *J. Geotech. Geoenviron. Eng.* 128(12), 1007-1017.

- 923 Youd, T.L., Idriss, I.M., Andrus, R.D., Arango, I., Castro, G., Christian, J.T., Dobry, R., Finn, W.L.,  
924 Harder Jr, L.F., Hynes, M.E. and Ishihara, K.(2001). Liquefaction resistance of soils: summary report  
925 from the 1996 NCEER and 1998 NCEER/NSF workshops on evaluation of liquefaction resistance of  
926 soils. *Journal of geotechnical and geoenvironmental engineering*, 127(10), pp.817-833.
- 927 Youd, T.L., and Perkins, D.M. (1978). Mapping liquefaction-induced ground failure potential, *Journal of*  
928 *the Geotechnical Engineering Division* 104, No. GT4, 433-446.
- 929 Youd, T.L., and Perkins, D.M. (1987). "Mapping of liquefaction severity index." *J. Geotech. Eng.*  
930 113(11), 1374-1392.
- 931 Zhang, G., Robertson, P. K., and Brachman, R. W. (2004). "Estimating liquefaction-induced lateral  
932 displacements using the standard penetration test or cone penetration test." *J. Geotech. Geoenviron.*  
933 *Eng.* 130(8), 861-871.